



## Coupled multiscale-modeling of microwave-heating-induced fracturing in shales

Guanglei Cui<sup>a</sup>, Tianyu Chen<sup>a,\*</sup>, Xiating Feng<sup>a</sup>, Zhongwei Chen<sup>b,\*\*</sup>, Derek Elsworth<sup>c</sup>, Hongwen Yu<sup>a</sup>, Xu Zheng<sup>d</sup>, Zhejun Pan<sup>e</sup>

<sup>a</sup> Key Laboratory of Ministry of Education on Safe Mining of Deep Metal Mines, Northeastern University, Shenyang, 110004, China

<sup>b</sup> School of Mechanical and Mining Engineering, The University of Queensland, St Lucia, QLD, 4074, Australia

<sup>c</sup> Department of Energy and Mineral Engineering, G3 Center and Energy Institute, The Pennsylvania State University, University Park, PA16802, USA

<sup>d</sup> Department of Civil Engineering, Liaoning Technical University, Fuxin, 123000, China

<sup>e</sup> CSIRO Energy Business Unit, Private Bag 10, Clayton South VIC, 3169, Australia

### ARTICLE INFO

#### Keywords:

Thermal stress  
Shear damage  
Tensile damage  
Intergranular fracture  
Transgranular fracture

### ABSTRACT

Microwave heating may be used to stimulate fracture formation and the release of hydrocarbons in gas shales. Although extensively studied experimentally and numerically, the microscopic observations are not fully explained in current work where the heating, at sample-scale, and fracturing, at the mineral-scale, are represented independently. Furthermore, the geometry, structure and mechanical interaction of different minerals are not fully considered in current approaches. We present a novel simulation approach to investigate the coupled electromagnetic-heating-stress-damage process. Microwave heating is simulated at sample-scale and the resulting stress-damage response is examined at micro-scale where minerals with contrasting thermo-mechanical characteristics are stacked as lamellae, instead of nested internally as in previous representations. A three-stage temperature evolution profile is observed in the shale samples – although some stages may be absent in other rocks. The mathematical model accounts for the three modes of stress generated between minerals: horizontal stress ( $\sigma_h$ ) (tensile stress parallel to the grain-grain interface) and the normal stress ( $\sigma_n$ ) (tensile stress normal to the grain-grain interface) applied on the minerals, and the shear stress ( $\tau$ ) applied on the interface between different minerals. The minerals comprising the shale matrix are categorized into three types – ‘high’, ‘intermediate’ and ‘low’ – conversion efficiency based on their susceptibility to thermal stressing from microwave irradiation. Shear damage and intergranular fracture usually occurs for minerals with high dielectric permittivity. Transgranular fracture may feature both in high permittivity minerals, due to the larger induced horizontal stress ( $\sigma_h$ ), and in low permittivity minerals - due to high volume fraction and larger size. The simulation approach is a powerful way to link the macro-scale characterization and heating to micro-mechanisms of rock failure. Also this work provides mineral classification and criteria to define a priori evaluation of the effectiveness of microwave treatment of shales and other mineral aggregates.

### 1. Introduction

High effectiveness reservoir stimulation technologies are needed for the commercial development of gas shale reservoirs<sup>1</sup> due to their ultra-low matrix porosity and permeability. Hydraulic fracturing is the current mainstream stimulation method, but presents several major shortcomings directly related to the use of water. These include impacts of water blocking and clay swelling which are suspected to damage the

reservoir and impair gas production.<sup>2,3</sup> Formation heat treatment (FHT) methods are effective in overcoming these disadvantages, and have been demonstrated to be a feasible approach to enhance gas production from unconventional oil/gas reservoirs.<sup>4,5</sup> FHT methods apply intense heat to the reservoir to vaporize host fluids, create overpressures, and to finally create new fractures. Conventional heating methods (e.g. electrical resistance heater, hot water flooding and high-temperature steam) are widely applied in the oil and natural gas industry. In these approaches,

\* Corresponding author. Key Laboratory of Ministry of Education on Safe Mining of Deep Metal Mines, Northeastern University, Northeastern University College of Resources and Civil Engineering, China.

\*\* Corresponding author.

E-mail addresses: [chentianyu@mail.neu.edu.cn](mailto:chentianyu@mail.neu.edu.cn) (T. Chen), [zhongwei.chen@uq.edu.au](mailto:zhongwei.chen@uq.edu.au) (Z. Chen).

<https://doi.org/10.1016/j.ijrmmms.2020.104520>

Received 6 March 2020; Received in revised form 25 September 2020; Accepted 12 October 2020

1365-1609/© 2020 Elsevier Ltd. All rights reserved.

heat is transferred by thermal conduction and convection, but restricted by geological conditions such as the presence of aquicludes and faults, preventing the transport of the hot liquids.<sup>6</sup> Different from these methods, microwave heating involves the conversion of the electromagnetic energy to heat.<sup>7,8</sup> It has been increasingly studied due to the following advantages<sup>9,10</sup>: (i) the thermal influence is projected far from the source since it is realized by energy conversion rather than heat transfer; (ii) heat generation is more efficient since it is fast, non-contact and projects volumetric heating; (iii) it is straightforward to implement in the field since it can instantly turned on, then off; and, most importantly, (iv) it has a high level of safety and is environmentally benign.

Microwaves are a form of electromagnetic waves with wavelengths in the range 1 mm to 1 m and frequencies varying between 300 MHz and 300 GHz.<sup>9,10</sup> Three cases occurred considering interactions of mineral with microwaves:<sup>11</sup> (1) microwave transparency, where microwaves penetrate but with little energy loss. Materials which are transparent to microwaves are classed as insulators and often used in microwave heating system as a warming cavity to support the material to be heated; (2) microwave absorption, where microwaves are adsorbed and converted into heat. Minerals featured with this characteristic also called absorbers and can be microwave heated; and (iii) microwave reflection and absorption. Metals with high conductivities reflect most microwaves and often adopted to retain the electromagnetic wave in the oven.<sup>12</sup> The interaction of materials with electromagnetic waves is described through dielectric permittivity,  $\kappa$ . In this, the dielectric permittivity,  $\kappa$ , is described as a conjugate function, as  $\kappa = \kappa_0(\kappa_r + i\kappa_i)$  where  $\kappa_r$  is the real part of the relative permittivity,  $\kappa_i$  is the imaginary part,  $\kappa_0$  defines the permittivity of a vacuum and  $i$  is the imaginary unit ( $-1^{1/2}$ ). The real part represents the ability to store electromagnetic energy and the imaginary part represents the ability to dissipate energy. Rocks are typically multi-mineralic aggregates with individual minerals presenting different responses to microwave radiation - some minerals adsorb radiation and some are microwave transparent.<sup>13</sup> The quartz and calcite are relatively unresponsive to microwave irradiation and can be treated as non-responsive phase.<sup>14</sup> While they would heat up because of the heat transfer. The phase transition in quartz and mineral decomposition of calcite would occur when temperature threshold values are obtained.<sup>15</sup> On the contrary, the pyrite has a high rate of absorption of microwave energy and the oxidative transformation would occur in the region of 350–700 °C.<sup>16</sup> The value of  $\kappa_i$  of some representative minerals are listed in Table 1 based on which the classification is made. These differences in the dielectric permittivities of adjacent minerals leads to a heterogeneous distribution of temperature and thermal stress. Furthermore, this classification criterion only considers the electro-magnetics parameters ignoring the thermodynamic and mechanical parameters which may lead to a poor judgement.

Key factors influencing microwave heating induced fracturing have been widely investigated.<sup>19,21</sup> The larger the applied microwave power and longer microwave irradiation time, the more significant in rock strength reduction.<sup>20,21</sup> However, there is a minimum microwave power density for a given mineralogy and mineral-aggregate texture below which no grain boundary damage is observed, regardless of the exposure time.<sup>19</sup> Understanding mechanisms of microwave heating induced fracturing has also attracts considerable attention through micro-scale characterizations - including SEM imaging<sup>20</sup> and macro-scale behaviors with experimental observations.<sup>21,22</sup> At micro-scale, differential linear and volumetric expansion will result between adjacent grains, due

to the different thermal expansion coefficients of the various minerals and the non-homogeneous distribution of dielectric permittivity of those minerals.<sup>21,22</sup> Stress concentrations are generated and will result in microcracking along crystal faces at the interface between adjacent minerals (*inter-granular*) or within the minerals (*trans-granular*). With an increase in irradiation time, microcracks will propagate and dilate, eventually causing failure and macroscopic fracture.<sup>23,24</sup> At macroscale, the temperature in the rock will increase rapidly after adsorbing the microwave radiation, expanding individual minerals and generating heterogeneous thermal stresses.<sup>25</sup> The rock sustains damage as the local tensile and shear stresses exceed the local threshold strengths. Therefore, both the tensile and shear stresses would result in the microwave irradiation induced damage of rock. The newly created fractures radially around adsorbing minerals are caused by the tensile stress, while fractures along the interface of between minerals are produced by shear stresses.<sup>26</sup>

In addition to experimental results and microscopic observations, a significant amount of numerical simulation studies have also been conducted to enhance overall understanding of the microwave heating induced damage process.<sup>27–29</sup> These studies fall into two groups. Early studies accommodated the behavior as decoupled between heating and damage.<sup>27,30</sup> Later studies fully coupled the electromagnetic-heating and thermal-stressing process.<sup>9,28</sup> In most applications the rock matrix is divided into two phases (adsorbing and transparent phases).<sup>26,27</sup> The thermal mismatch between the two mineral-types results in a large localized thermal stress surrounding absorber minerals.<sup>27,29</sup> In recent studies,<sup>15,29,31</sup> maximum tensile stress, maximum principal stress, von Mises stress, and Tresca yield stress criteria are applied as failure criteria.

Although extensively studied, both experimentally and numerically, significant knowledge gaps still endure: (1) microscopic observations are not fully explained by the current theoretical and numerical models as the mechanisms of intergranular fracture and transgranular fracture are poorly understand and the appearances of radial fractures and circular fractures are not well predicted; (2) the adsorbing and transparent phases are assumed circular and mutually embedded as core and surrounding carapace – representing an incomplete representation of real rocks that are closer to lamellar in structure – and will have significantly different thermal and mechanical interaction if this geometric reality is not accommodated; (3) the heating process at the macro-scale and fracturing process at the mineral scale are stimulated separately; and (4) the selected failure criteria can hardly represent the micro-structure of minerals as the impacts of the geometric topology of minerals are poorly treated.

These key knowledge gaps prescribe the focus of the following study. We propose an improved simulation approach to investigate the electromagnetic-heating-stress-damage process in heterogeneous multi-mineralic aggregates with coupled macroscopic heating linked to microscopic thermal damage. In the macro-model, the microwave heating process is simulated at sample scale using the Helmholtz equation accommodating electromagnetic loss. Complementarily, the stress-damage process is simulated at the mineral/micro-scale in which minerals with contrasting dielectric/thermal-expansion characteristics are stacked as lamellae, rather than nested as in previous work. A mathematical model is then established to account for the micro-scale fracturing process. The heating process, at the sample scale, and the fracturing process, at the mineral scale, are therefore fully coupled and

**Table 1**  
The  $\kappa_i$  value of some representative minerals.<sup>17,18</sup>

Minerals	Plagioclase	Pyroxene	Ilmenite	Pyrite	Classification
$\kappa_i$	0.004–0.32	1.62	32.58	0.4–3	Adsorbing
Minerals	Quartz	Orthoclase	Muscovite	Calcite	
$\kappa_i$	0.0006–0.0033	0.00019	0.0006–0.0034	0.005	Poorly Absorbing

simulated. Highly constrained observations from a microwave heating experiment on shale is used to verify the results obtained from macro-model – including corroboration against SEM observations to verify modes of intergranular and transgranular fractures.

## 2. Governing equations for coupled electromagnetic-heating-stress-damage model

We introduce the constraints and capabilities of the fully coupled theoretical model. The model incorporates: (1) propagation of the electromagnetic field, including electromagnetic loss and heat transfer applied at sample scale, and (2) a governing equation for microwave heating induced stress and rock damage at the mineral scale.

### 2.1. Electromagnetic field

Maxwell's Equation defines the electromagnetic wave propagation process.<sup>9,10</sup> Maxwell's equation describes how electric and magnetic fields are generated by charges, currents, and changes of the fields. It comprises four sub-equations: Gauss's Law for electric fields describing the relationship between a static electric field and electric charge; Gauss's law for magnetic fields, stating that there are no "magnetic charges"; the Maxwell-Faraday Equation describing how a time varying magnetic field creates electric charge; and the Maxwell-Ampere Law stating that magnetic fields can be generated in two ways - by an electric current and by a changing electric field. These may be defined in differential form as:

$$\text{Gauss's Law for electric fields: } \nabla \cdot D = \rho_e \quad (1)$$

$$\text{Gauss' Law for magnetic fields: } \nabla \cdot B = 0 \quad (2)$$

$$\text{Maxwell – Faraday Equation: } \nabla \times E_e = -\frac{\partial B}{\partial t} \quad (3)$$

$$\text{Maxwell – Ampere's Law: } \nabla \times H = J + \frac{\partial D}{\partial t} \quad (4)$$

where  $\nabla$  denotes the nabla symbol;  $\nabla \cdot$  represents the divergence oper-

ator;  $\nabla \times$  denotes a curl operator;  $E_e$  denotes electric field,  $V/m$ ;  $B$  represents the magnetic field,  $Wb/m^2$ ;  $\rho_e$  represents the electric charge density,  $C/m^3$ ;  $D$  is the electric displacement or electric flux density,  $C/m^2$ ;  $H$  is magnetic intensity,  $A/m$ .  $J$  is the current density,  $A/m^2$ . In addition, the following equation describes the relationship between  $D$  and  $E_e$ , and  $B$  and  $H$ :

$$D = \kappa_0(\kappa_r + i\kappa_i)E_e, B = \mu_0\mu_r H_r, \text{ and } J = \sigma_E E_e \quad (5)$$

where  $\kappa_0$  denotes the permittivity of the free space ( $8.854187817 \times 10^{-12}$  F/m),  $\mu_0$  represents the magnetic permeability of free space ( $1.2566370614 \times 10^{-6}$  H/m),  $\mu_r$  is the relative magnetic permeability,  $\sigma_E$  is the electrical conductivity,  $S/m$ .

Substituting Eq. (5) into the Maxwell Equation (Eq. (1)~ (4)), the Helmholtz vector equation results, as:<sup>32</sup>

$$\nabla \times \mu_r^{-1}(\nabla \times E_e) - k_0^2 \left( \kappa_r - \frac{i\sigma_E}{\omega\kappa_0} \right) E_e = 0 \quad (6)$$

where  $k_0 = \omega/c_0$  is the free space wave number,  $c_0$  is the speed of light in a vacuum ( $2.998 \times 10^8$  m/s), and  $\omega = 2\pi f$  is the angular frequency, (rad/s). In the implementation process, Eq. (6) is applied and solved.

### 2.2. Heat transfer

Under the assumption that (1) the inter-convertibility of thermal and mechanical energy is neglected, (2) the formation porosity is a minor proportion of the bulk volume and can be neglected, and that (3) interstitial fluids filling this porosity are correspondingly proportionately small, as is the case in typical shale reservoirs, Fourier's law for conductive heat transfer may be applied to describe the microwave induced heating and heating transfer process in an REV, as:<sup>33</sup>

$$\rho_s C_p \frac{\partial T}{\partial t} + \rho_s C_p u \nabla T + \nabla \cdot q = Q_{wave} \quad (7)$$

where  $\rho_s$  denotes the density of shale sample,  $kg/m^3$ ;  $C_p$  represents the specific heat capacity,  $J/(kg \cdot K)$ , and  $T$  represents the temperature,  $K$ . Heat flux  $q(W/m^2)$  is expressed as:

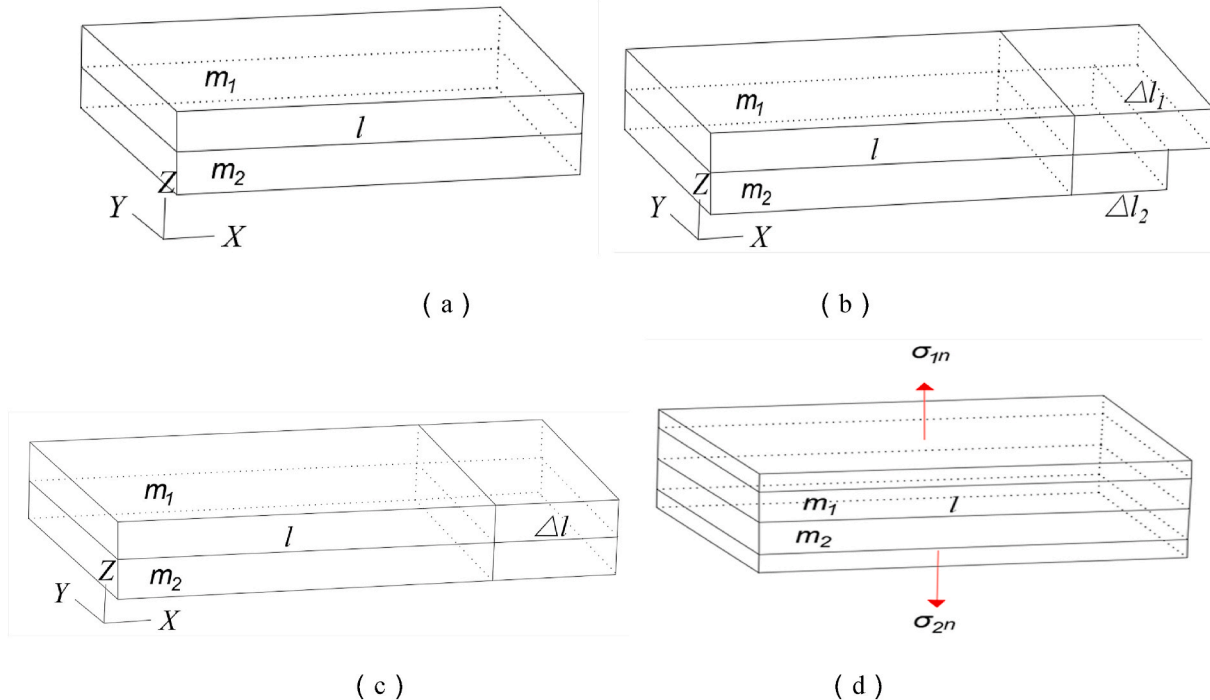


Fig. 1. Schematic of proposed mineral damage process: (a) initial state; (b) free swelling state; (c) final state; (d) induced normal stress.

$$q = -k_T \nabla T \quad (8)$$

where  $k_T$  is the thermal conductivity, ( $W/(m^*K)$ ). When penetrating a dielectric material with electromagnetic loss, the microwave energy is absorbed and part of the microwave energy is converted into the heat energy which serves as a heat source  $Q_{wave}$  ( $W/m^3$ ):<sup>9,34</sup>

$$Q_{wave} = \frac{\omega \kappa_0 \kappa_i |\mathbf{E}_e|^2}{2} \quad (9)$$

which may be substituted directly as a volumetric source in Eq. (7) to define the heating of the material.

### 2.3. Microwave heating-induced stress

The main minerals in the shale are quartz, clay, pyrite, dolomite, feldspar and calcite.<sup>35</sup> The multi-mineralic geometry is apparent at micrometer scale with most minerals are arranged in a parallel distribution rather than internally nested within individual grains. These observations are also apparent in other work.<sup>36</sup>

Based on the above observations, we established a micro-scale (micrometer scale) discrete model to represent the heterogeneous stress distribution that will develop between pairs of adjacent minerals as a direct consequence of microwave heating. Fig. 1(a) shows two adjacent minerals of contrasting compositions, labelled as  $m_1$  and  $m_2$ . These are vertically stacked with a length of  $l$  in the x direction, width of  $w$  in the y direction and height of  $h_1$  and  $h_2$  in the z direction. The initial temperature is  $T_0$ , and we assume that no relative slippage and bending occur during the heating process. For the boundary conditions, it is assumed that the left face is fixed in the x- and y-directions and the interface between the two minerals is fixed in the z-direction. Therefore the right face is free to extend in the x- and y-directions, and the top and bottom can extend along all three directions. After microwave heating, the temperatures of two minerals are raised to  $T_1$  and  $T_2$  due to their contrasting dielectric permittivities.

In this work, it is assumed that  $T_1 > T_2$  and  $\alpha_1 > \alpha_2$  where  $\alpha$  represents thermal expansion coefficient. If there is no constraint for the thermal expansion on the right side (free swelling state) (Fig. 1(b)), we have:

$$\Delta l_1 = \alpha_1 (T_1 - T_0) l \cdot \text{and} \cdot \Delta l_2 = \alpha_2 (T_2 - T_0) l \quad (10)$$

Also we can obtain that the expansion increment of mineral  $m_1$  is larger than that of mineral  $m_2$  ( $\Delta l_1 > \Delta l_2$ ), as shown in Fig. 1(b). As assumed, no relative slippage occurs at the interface and the lengths of the two minerals may change but remain the same at the final state, as shown in Fig. 1(c). In such a condition, the actual extended length of mineral  $m_1$  is smaller than that in the free expansion state and the actual extended length of mineral  $m_2$  is larger than that in the free expansion state. In other words, mineral  $m_1$  is compressed by a strain of  $\varepsilon_1 = \sigma_{1h}/E_1$  and length changes as  $\varepsilon_1 l = \sigma_{1h} l / E_1$ ; and mineral  $m_2$  is stretched with a strain of  $\varepsilon_2 = \sigma_{2h}/E_2$  and extends as  $\varepsilon_2 l = \sigma_{2h} l / E_2$ , in which  $E$  represents the deformation modulus,  $\sigma_{1h}$  and  $\sigma_{2h}$  are the horizontal stresses in minerals  $m_1$  and  $m_2$ . Following the above analysis, we obtain the final lengths of minerals  $m_1$  and  $m_2$  as:

$$\alpha_1 (T_1 - T_0) l + \varepsilon_1 l = \alpha_1 (T_1 - T_0) l + \sigma_{1h} l / E_1 \cdot \text{and} \cdot \alpha_2 (T_2 - T_0) l + \varepsilon_2 l = \alpha_2 (T_2 - T_0) l + \sigma_{2h} l / E_2. \quad (11)$$

In the final equilibrium state, the lengths of  $m_1$  and  $m_2$  are equal as shown in Fig. 1(c) as no relative slippage and bending occur during the heating process:

$$\alpha_1 (T_1 - T_0) l + \sigma_{1h} l / E_1 = \alpha_2 (T_2 - T_0) l + \sigma_{2h} l / E_2. \quad (12)$$

Also the force in the final state are equal:

$$\sigma_{1h} A_1 = \sigma_{2h} A_2 \quad (13)$$

in which  $A_1$  and  $A_2$  represent the areas in the YZ plane of minerals  $m_1$  and  $m_2$ , with  $A_1 = w \times h_1$  and  $A_2 = w \times h_2$ .

#### (a) Horizontal Stress

The stress state in two stacked and bonded minerals subjected to microwave heating are analyzed as above, with the stresses in different directions obtained as introduced below. Based on Eqs. (12) and (13), we can obtain the horizontal stresses  $\sigma_{1h}$  and  $\sigma_{2h}$  as:

$$\sigma_{1h} = -\eta \alpha_1 (T_1 - T_0) E_1 \cdot \text{and} \cdot \sigma_{2h} = \eta \alpha_1 (T_1 - T_0) E_1 \frac{A_1}{A_2} \quad (14)$$

in which  $\eta$  is a restraint coefficient, defined as:

$$\eta = \left( 1 - \frac{\alpha_2 (T_2 - T_0)}{\alpha_1 (T_1 - T_0)} \right) / \left( 1 + \frac{A_1 E_1}{A_2 E_2} \right) \quad (15)$$

When  $\eta > 0$ ,  $\sigma_{1h} < 0$  and a compressive stress results;  $\sigma_{2h} > 0$  and is a tensile stress. When  $\eta < 0$ , the opposite situation is resulted.

#### (b) Normal Stress

The thermal stresses induced along the z direction (normal stress) would also be defined. Mineral  $m_1$  will expand in the z direction as shown in Fig. 1(d) and we have:

$$\sigma_{1n} A_1 = \sigma_{1n} S_1 \cdot \text{and} \cdot \sigma_{1n} = \frac{\sigma_{1h} A_1}{S_1} \quad (16)$$

in which  $S_1$  represents the area of mineral  $m_1$  on the XY plane with  $S_1 = wl$ . Further simplifying this yields:

$$\sigma_{1n} = \sigma_{1h} \frac{h_1}{l} \quad (17)$$

Similarly, we have

$$\sigma_{2n} = \sigma_{2h} \frac{h_2}{l} \quad (18)$$

#### (c) Shear Stress

Shear stress develops along the interface between two minerals as the horizontal strains evolving within the adjacent minerals are different. For the mineral  $m_1$ , the tensile force along the x-direction is  $F_1 = \sigma_1 w h_1$  and for mineral  $m_2$ ,  $F_2 = \sigma_2 w h_2$ . The resulting shear stress on the interface between the two minerals is:

$$\tau = \frac{F_1 - F_2}{wl} \quad (19)$$

In the above analysis,  $F_1$  and  $F_2$  are of opposite sense, and are of positive and negative sign representing tensile and compressive forces, respectively. Therefore in Eq. (19) the two terms are additive for their

absolute values. Thus, we have:

$$\tau = \frac{|\sigma_1 w h_1| - |\sigma_2 w h_2|}{wl} = \frac{\left| \sigma_1 \frac{w h_1}{w h_1} \right| + \left| \sigma_2 \frac{w h_2}{w h_1} \right|}{\frac{wl}{w h_1}} = \frac{|\sigma_1| + \left| \sigma_2 \frac{A_2}{A_1} \right|}{\frac{wl}{w h_1}} = \frac{2|\sigma_1|}{\frac{l}{h_1}} \quad (20)$$

## 2.4. Mineral damage model

As illustrated above, the microwave-heating-induced stress on the minerals can be categorized into three forms: compressive, tensile and shear stresses. As shown previously, mineral  $m_1$  is compressed at the x-direction and extended in the z-direction; Mineral  $m_2$  is extended in both x- and z-directions but with a resulting shear stress on the interface between the two minerals. In this section, the damage criteria and stress-strain behavior following damage are introduced.

The maximum tensile/compressive/shear stress criterion is selected to determine the failure mode (tension, compression, or shear modes), which can be defined from:

$$F_i \equiv \sigma_i - f_{i0} = 0 \quad (21)$$

where  $f_{i0}$  represents the uniaxial tensile, compressive or shear strength ( $i = t, c$  and  $s$ ), and  $F_t, F_c$  and  $F_s$  are three damage threshold functions used to link tensile, compressional and shear damage.

After damage, the elastic modulus of an element degrades monotonically as damage evolves and is related to the damage variable,  $D$  ( $0 < D < 1$ ):<sup>37,38</sup>

$$E = (1 - D)E_0 \quad (22)$$

where  $E$  denotes the elastic moduli and subscript 0 represents the undamaged state. A power function is used to describe the softening process in the post-peak region. Thus, the damage variable  $D$  can be defined as:<sup>38,39</sup>

$$D = \begin{cases} 0 & \varepsilon < \varepsilon_{i0} \\ 1 - \left| \frac{\varepsilon_{i0}}{\varepsilon} \right|^n & \varepsilon_{i0} < \varepsilon < \varepsilon_{ir} \\ 1 - \left| \frac{\lambda_i \varepsilon_{i0}}{\varepsilon} \right|^n & \varepsilon_{ir} < \varepsilon < \varepsilon_{iu} \\ 1 & \varepsilon_{iu} < \varepsilon \end{cases} \quad (23)$$

where the subscript  $i$  represents shear ( $s$ ), compressive ( $c$ ) or tensile ( $t$ ) strains.  $\varepsilon_{i0}$  denotes the compressive strain at the elastic limit;  $\varepsilon_{iu}$  represents the ultimate strain,  $\lambda_i$  denotes residual strength coefficient defined as the ratio of the residual strength  $f_{ir}$  to the initial strength of the rock  $f_{i0}$ , and  $\varepsilon_{ir}$  represents the strain corresponding to the residual strength  $f_{ir}$ ;  $n$  denotes a constitutive coefficient assumed as 2 in this work. The typical stress-strain relationship is illustrated in Fig. 2.

## 3. Implementation of numerical model

We developed a fully coupled electromagnetic-heating-stress-damage model using COMSOL Multiphysics (Version 5.4). The

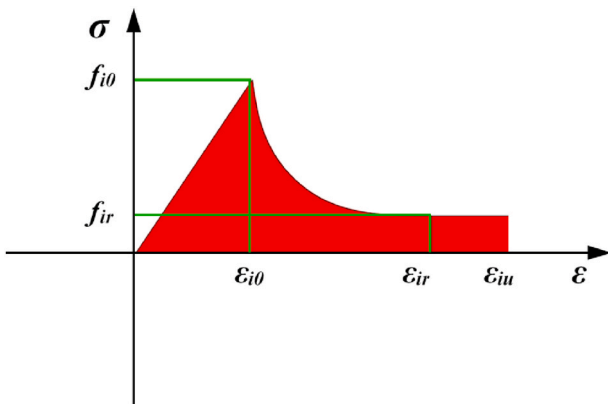


Fig. 2. Idealized stress-strain-damage relationship,<sup>40</sup>  $i$  represents shear ( $s$ ), compressive ( $c$ ) or tensile ( $t$ ) strains.

modeling process is introduced as follows.

## 3.1. Computational approach

Three key features are considered in the modeling – the microwave oven itself (void), the shale sample and the proposed discrete model. The microwave oven and shale sample are at centimeter scale while the discrete model is at micrometer scale. Thus separate but linked models are needed to avoid a scale mismatch problem and meshing difficulties/inconsistencies. To avoid this issue, two different scale simulation models are established – a macro-model at the centimeter scale and a micro-model at the micrometer scale.

In the macro-model, both the microwave oven and sample are represented, and the electromagnetic-heating coupled process is simulated. The propagation of microwaves is a transient process at the scale of nanosecond (ns) while the heating process is slow, on the order of seconds (s) or minutes (m). This mismatch in timescales is avoided by first solving Maxwell's Equation in the frequency domain using the Helmholtz Equation (Eq. (6)). Then the microwave heating process is solved with Eq. (9) by returning this to the time domain. These two equations are solved simultaneously.

In the micro-model, a discrete model is established to calculate the mechanical interaction between different minerals and to represent the heating-stress-damage coupled process. From the macro-model, the distribution of electric field ( $E_e$ ) of the entire sample is known. Any infinitesimally-small volume (approaching to a point) of the sample is selected and we assumed that: (1) the small volume comprises a discrete model, and (2) the electric field ( $E_e$ ) on the representative elemental volume (REV) is uniform. Under these assumptions, an extrusion function is applied to transfer the electric field ( $E_e$ ) of the small volume on the entire sample to the micro discrete model<sup>41</sup> with Eq. (9) applied to represent the heating process. Coupling with the heating-stress is achieved with Eqs. (14)~(20). Damage is realized as the Young's modulus is assumed to decline step by step until it approaches to zero. The damage criterion is evaluated via MATLAB. Once the criterion is reached, a declined Young's modulus is evaluated according to Eq. (23) and applied within the COMSOL model. The coupled processes and feedbacks together with the workflow are illustrated in Fig. 3.

## 3.2. Model geometry

The macro-scale model is established based on the microwave-heating case in the application library of COMSOL Multiphysics.<sup>42</sup> The microwave oven, waveguide and shale sample are all included in the model in which the shale sample sits bottom-center within the microwave oven. The oven cabinet is prismatic with a length of 329 mm, width of 315 mm and height of 180 mm; The waveguide is also prismatic with dimensions of 50 mm (L)  $\times$  50 mm (W)  $\times$  70 mm (H). The cylindrical sample is 50 mm in diameter and 100 mm in height. The relative position and sizes of the three objects are shown in Fig. 4(a). For the meshing, the physics-controlled mesh is applied to the macro-model with a maximum element size of 1/5 of the wavelength. Mesh size is predefined as a fine mesh. After meshing, there are 475509 elements in the entire geometry with an average element quality of 0.83.

The micro-model is established based on the theoretical model proposed in Section 2.3, accommodating two contrasting and adjacent minerals. Minerals comprising the shale matrix are usually at micrometer scale, ranging from one hundred nanometers to 10  $\mu$ m. For simplicity, we assume that the two minerals are both rectangular/prismatic and have the same size with a length of 10  $\mu$ m, width of 5  $\mu$ m and height of 2  $\mu$ m. In the micro-model, the strain and stress are selected as the key criterion and the scale effects are ignored. For the meshing, the sweep method is applied because of its regular geometry and the size is predefined as extra fine. After meshing, 8004 elements comprise the geometry with an average element quality of 0.95.

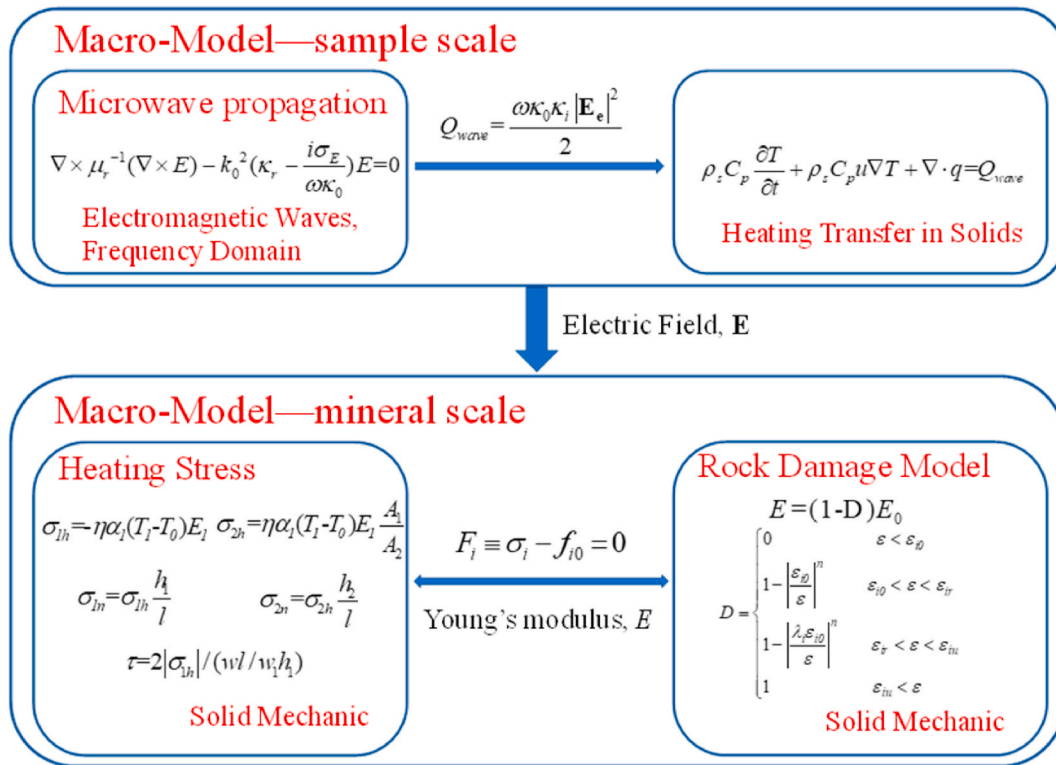


Fig. 3. Coupling and feedbacks accommodated in the simulation approach.

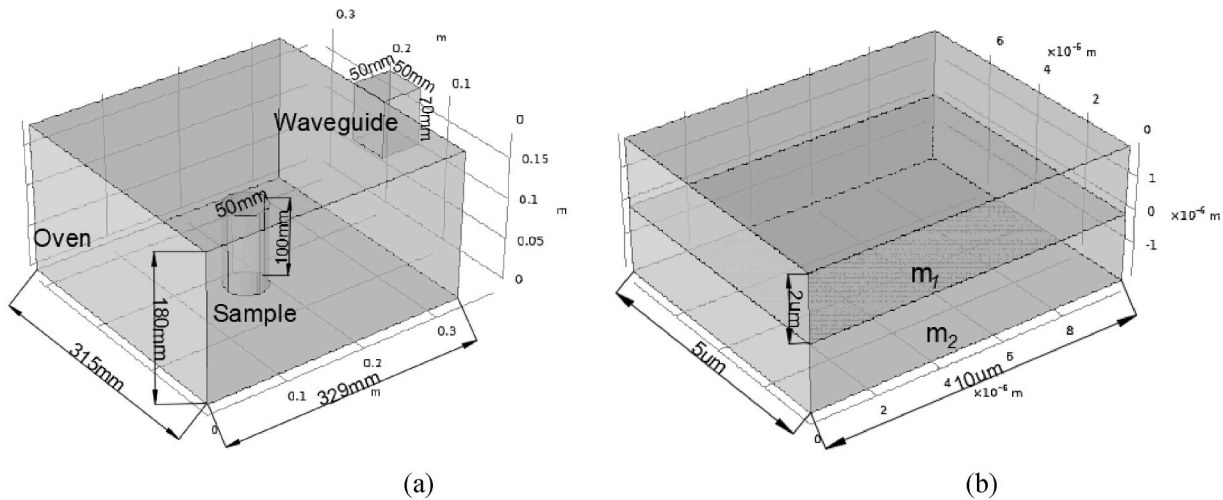


Fig. 4. Geometry of the simulation model at both (a) macro- and (b) micro-scales.

### 3.3. Input parameters and boundary conditions

The coupled microwave heating process is simulated in the macro-model using microwave propagation in both sample and oven with only the heating process simulated in the sample. To achieve this, the boundary conditions for the electromagnetic wave propagation module are assigned as follows: (1) an impedance boundary is applied at the walls of the oven to ensure that the electromagnetic energy is retained within the oven; and (2) a prismatic port boundary is applied at the entrance of the wave guide serving as the source of the electromagnetic radiation. The boundary conditions of the heat transfer module are set as: (1) a thermal insulation boundary condition is assigned to the base; and (2) a convective heat transfer boundary is applied to all other faces.

The coupled heating-stress-damage process is applied in the micro-

model in which thermal-stressing is represented in COMSOL Multiphysics and the damage process is represented in MATLAB. To achieve these goals, heat transfer and solid mechanics modules are linked in COMSOL Multiphysics, and a link between COMSOL and MATLAB is applied to check the damage criterion. For heat transfer within the solid module, the microwave heating is identified as the heating source. The application and linkages between feedbacks in the COMSOL modules are illustrated in Fig. 3.

### 4. Results and analysis of macro-model

The results of the macro-model are validated against a microwave heating experiment conducted on shale. Parametric studies investigate the impacts of the temperature-dependent specific heat capacity and

permittivity on the microwave heating process. These details are introduced in the following.

#### 4.1. Comparison with experiment results

##### 4.1.1. Experiment method and observations

The microwave heating experiment is conducted on shale collected from an outcrop of the Longmaxi formation in Changning County, Yibin City, Sichuan Province. The principal minerals in the shale are quartz, clay and calcite, as shown in Table 2. The shale block sample was drilled to yield a cylinder with a height of 100 mm and diameter of 50 mm as shown in Fig. 6(a). All samples were dried under vacuum for >72 h at the 50 °C before microwave heating to eliminate the impact of environmental water. A household microwave oven (Galanz, G70F20CN1L-DG(B0)) is applied with a constant power of 700 W and the waveguide is located at the top of the right side.

The microwave irradiation time was increased step by step. After the microwave irradiation is applied for the first time step, the sample is taken out of the microwave oven and the temperature slowly lowered to 90 °C (simulating a return to reservoir temperature). Then the next microwave radiation step is performed, and the time of microwave heating in the next step will be 30 s longer than that in the previous step. Before and after each microwave heating step, the temperature on the top surface of the sample is determined by a Fluke infrared thermometer (model: 568-2) with an accuracy of  $\pm 1$  °C. The irradiation process continued for 50 min. The shale sample after microwave heating is shown in Fig. 6 (b) with some micro-fractures developing but remain intact.

##### 4.1.2. Verification process and results

The temperature obtained from the macro-model is validated against the experimental results. Permittivity was not measured in our experiment, with this being referenced to prior work,<sup>43</sup> establishing a relationship between permittivity with temperature ( $\kappa$ - $T$  curve,  $f_{\kappa}(T)$ ) to fit the experimental data (Fig. 5(a)). As show in this figure, both real and imaginary parts of the permittivity are near constant with a small reduction below 800 K and increase rapidly above 800 K. The small reduction is related to the evaporation of retained water and the details is discussed later. While the increase is attributed to the organic matter. The related literature suggested that the polar molecules in the organic fraction started to mobilize increasing the dielectric properties when the temperature reaches a threshold value<sup>44</sup> and the increment is proportional to the TOC content.<sup>43</sup>

Specific heat capacity ( $C_p$ ) is another important parameter controlling microwave heating. It links heating potential to delivered energy and usually increases with temperature for a specific material.<sup>13</sup> A distinct rise of heat capacity is apparent in quartz-rich rocks when the quartz transforms from  $\alpha$ -phase to  $\beta$ -phase.<sup>45</sup> This peak is apparent in the narrow temperature range bracketing the phase-transformation temperature with the specific heat capacity returning to the baseline curve after the brief excursion at the peak. A relationship between specific heat capacity and temperature is established ( $C_p$ - $T$  curve,  $f_{C_p}(T)$ ) to fit the experiment results shown in Fig. 5(b). The initial value of the assumed specific heat capacity is smaller than the curve in Hartlieb work<sup>45</sup> while the peak value is more significant because of the existence of water. The details are discussed later.

The other parameters are listed in Table 3. The comparisons of simulation results with experimental data are shown in Fig. 6(c). The

**Table 2**

Mineralogical composition of shale samples.

Mineral compositions (%)						TOC (%)	R <sub>o,max</sub> (%)
Quartz	Feldspar	Pyrite	Clay minerals	Calcite	Dolomite		
32.45	3.42	3.13	18.57	32.16	8.02	2.24	2.41

temperature is reported as the averaged value of the top surface. Goodness-of-fit (Regression coefficients,  $R^2$ ) is used to illustrate the fidelity of the fitting results - its value is 0.95 indicating a satisfactory fitting result.

#### 4.2. Impacts of specific heat capacity on microwave heating

To investigate the impacts of the specific heat capacity ( $C_p$ ) on the microwave heating process, five scenarios are designed as follows.

Scenario I: The  $C_p$ - $T$  relationship in Fig. 5(b) is applied for specific heat capacity and the peak because of the mineral phase transition is considered, labelled as  $f_{C_p}(T_{peak})$ ; Scenario II: The  $C_p$ - $T$  relationship in Fig. 5(b) is applied but the peak is neglected, labelled as  $f_{C_p}(T_{non-peak})$ ; Scenario III: The specific heat capacity is considered as a constant value with a geometric average value applied as:

$$C_{pIII} = \frac{\int_{T_{min}}^{T_{max}} f_{C_p}(T_{peak}) dT}{T_{max} - T_{min}} \quad (24)$$

in which the numerator represents the area integral of specific heat capacity ( $C_p$ ) with temperature ( $T$ ) and the denominator represents the temperature range.

Scenario IV: The specific heat capacity is a constant and the arithmetic average value is applied as:

$$C_{pIV} = \frac{C_{pmax} + C_{pmin}}{2} \quad (25)$$

in which  $C_{pmax}$  denotes the maximum value of the specific heat capacity and  $C_{pmin}$  denotes the minimum value. In all scenarios in this section, the  $\kappa$ - $T$  relationship of Fig. 5 (a) is applied for dielectric permittivity. It should be noted that the specific heat capacities are constant for Scenarios III and IV with  $C_{pIV}(3520 \text{ J/(kg}\cdot\text{T)}) > C_{pIII}(1350 \text{ J/(kg}\cdot\text{T)})$ .

To clearly illustrate the impacts of  $C_p$  on the evolving temperature, we report the maximum value and minimum value of temperature of the whole sample shown in Fig. 7. As shown in Scenario I, three heating stages can be observed: Stage I, Stage II and Stage III. In Stage I, the temperature increases with the irradiation time due to the low value of  $C_p$ . In Stage II, the temperature increases only slowly or remains constant with irradiation time due to increasing  $C_p$ . In Stage III, the temperature suddenly increases (>800 K) due to the increased permittivity and the finish of mineral phase transition. Although, only the first two stages are observed in our experimental work, because of the short microwave heating time, the entire microwave heating process, including all three stages, is apparent in other work.<sup>46,47</sup>

Comparing Scenarios I and II, we find that the variations in temperature are similar for the first stage while Scenario I takes more time to reach the third stage due of the existence of  $C_p$ -peak because of energy adsorption induced by the phase transition - the  $C_p$  -peak is a potential trough, with additional energy expended in transiting this trough. For constant specific heat capacity (Scenarios III~IV) the temperatures increase near-linearly with time and lower  $C_p$  results in an increased temperature. Stage III is not apparent for Scenario IV due to its larger specific heat capacity prohibiting the temperature to reach the point where permittivity suddenly increases.

#### 4.3. Impact of dielectric permittivity on microwave heating

As discussed above, the permittivity can be divided into both real

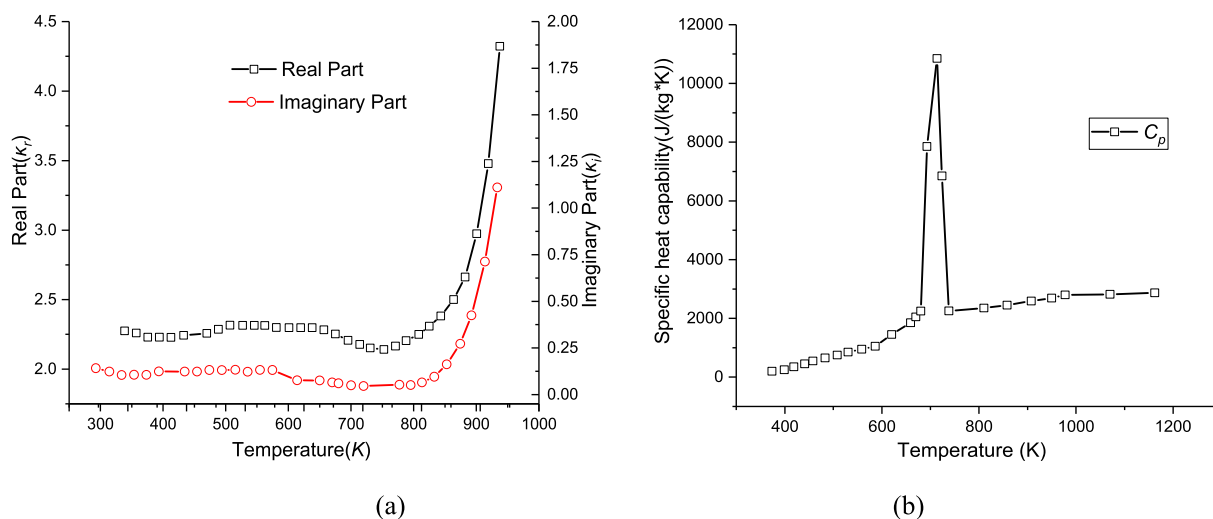


Fig. 5. Relationship of (a) permittivity and (b) specific heat capacity with evolving temperature.

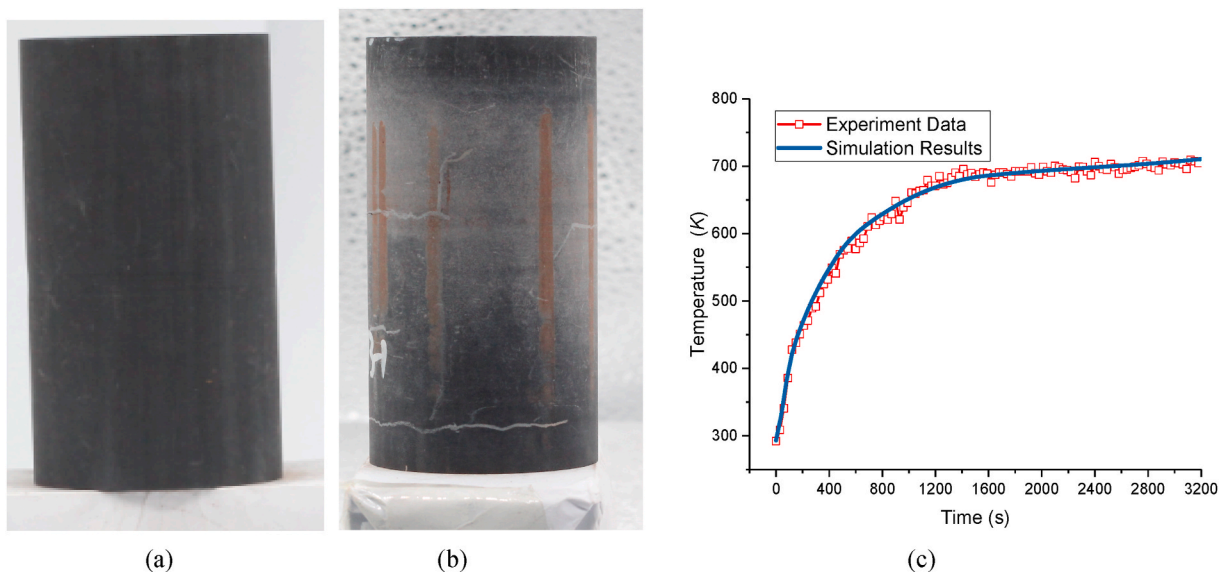


Fig. 6. (a) sample before microwave heating, (b) sample after microwave heating and (c) fitted results with temperature.

Table 3  
Input parameters for microwave heating simulations of the shale sample.

Physical property	Value	Unit	Physical property	Value	Unit
Microwave frequency	2.45	GHz	Microwave power	700	W
Oven size (cuboid)	329 × 315 × 180	mm	Guide size (cuboid)	50 × 50 × 70	mm
Sample size (cylinder)	100(h) × 50(d)	mm	Sample Density	2600	kg/m <sup>3</sup>
Dielectric constant (κ <sub>r</sub> )	Fig. 5 (a)		Loss factor (κ <sub>i</sub> )	Fig. 5 (a)	
Heat conductivity of sample	2.5	W/(m × K)	Initial temperature	300	K
Specific heat capacity	Fig. 5 (b)	J/(kg × K)	Dielectric constant of air	1	

and imaginary parts with both increase sharply above 800 K. We construct three scenarios to investigate the impacts of the permittivity on the microwave heating process with the C<sub>p</sub>-T relationship of Fig. 5(b)

(f<sub>cp</sub>(T<sub>peak</sub>)) applied for specific heat capacity. The details are listed as follows.

Scenario I: The κ-T relationship of Fig. 5 (a) is applied to represent permittivity.

Scenario II: The κ-T relationship of Fig. 5 (a) is applied for permittivity, but the increase of the imaginary part above 800 K is ignored.

Scenario III: The κ-T relationship of Fig. 5 (a) is applied for permittivity, but the increase of the real part above 800 K is ignored.

We report the maximum and minimum values of temperature within the entire sample for different dielectric permittivities in Fig. 8. Both Stages I and II are observed in all scenarios while the suddenly increase stage (Stage III) is not displayed for Scenario II. The sudden increase stage (Stage III) also appears in Scenario III, but with an apparent time lag. In other words, the increase in the imaginary part of the dielectric permittivity is the main contribution to the sudden increase in temperature above 800 K. Compared with imaginary part, the real part has a smaller impact on the microwave heating process. Our recent research<sup>48</sup> also implied that the real part not only changes the value of the electric field intensity but also the field distribution and therefore the impact of the real part of dielectric permittivity is not universal.

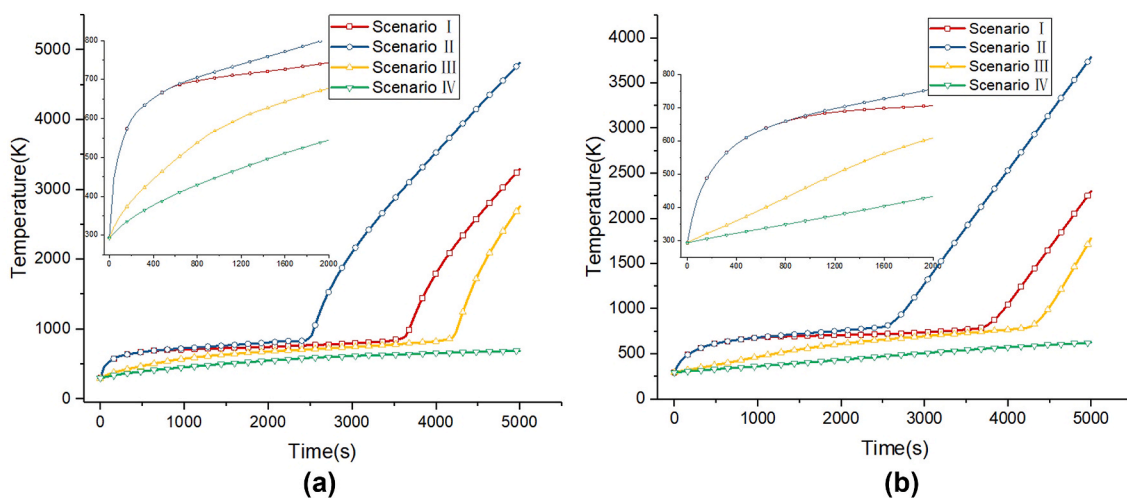


Fig. 7. Variation in generated temperature histories for different specific heat capacities: (a) maximum temperatures, and (b) minimum temperatures.

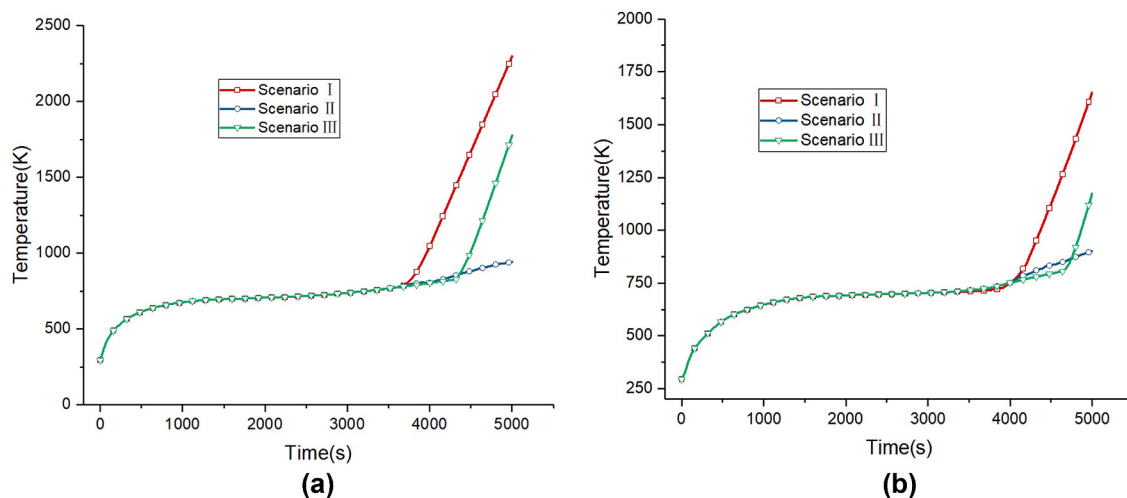


Fig. 8. Variation in temperature history for different permittivities: (a) maximum and (b) minimum temperatures.

## 5. Results and analysis of micro-model

In this section, the results of the micro-model are presented. The responses of different minerals within the shale matrix to the microwave irradiation and the resulting thermal stresses are first investigated – providing the key data to define the mechanical interaction between different minerals.

### 5.1. Thermodynamics and mechanical parameters of different minerals

As noted above, the specific heat capacity ( $C_p$ ) and dielectric permittivity ( $\kappa$ ) play a key role in the microwave heating process. The dielectric permittivity of different minerals are listed in Table 4. The permittivities of pyrite and quartz are particularly temperature-dependent, as shown in Fig. 9(a) and (b). The specific heat capacities of minerals also vary with temperature as shown in Fig. 9 (c). The thermal expansion coefficients of different minerals are

shown in Fig. 9 (d) and their thermal conductivities in Fig. 9 (e). In addition to these thermodynamic properties, their mechanical properties are also important, as they define the evolving stress-strain state of the mineral pairs. The bulk moduli of different minerals are shown in Fig. 9 (f) with the other relevant mechanical parameters listed in Table 5.

### 5.2. Responses of different minerals to microwave heating

Different minerals have contrasting thermodynamic and mechanical parameters. Therefore their response to electromagnetic irradiation at the same power, duration, mode and frequency are totally different. Fig. 10 shows the results of variations of microwave-heating-induced stress with time for different minerals, evaluated from the product  $K\alpha\Delta T$  in which  $K$  is the bulk modulus and damage is not considered. In the figure, the heating stress in pyrite corresponds to the right axis that for the other minerals corresponds to the left axis.

Table 4  
Thermodynamic properties of minerals comprising the shale matrix.

	Quartz <sup>51</sup>	Feldspar <sup>17</sup>	Pyrite <sup>16</sup>	Clay <sup>49</sup>	Calcite <sup>18</sup>	Dolomite <sup>18</sup>
Real Part	Fig. 9 (a)	5.52	Fig. 9 (b)	4	9.2	7.41
Imaginary Part	Fig. 9 (a)	0.01	Fig. 9 (b)	0.2	0.005	0.02

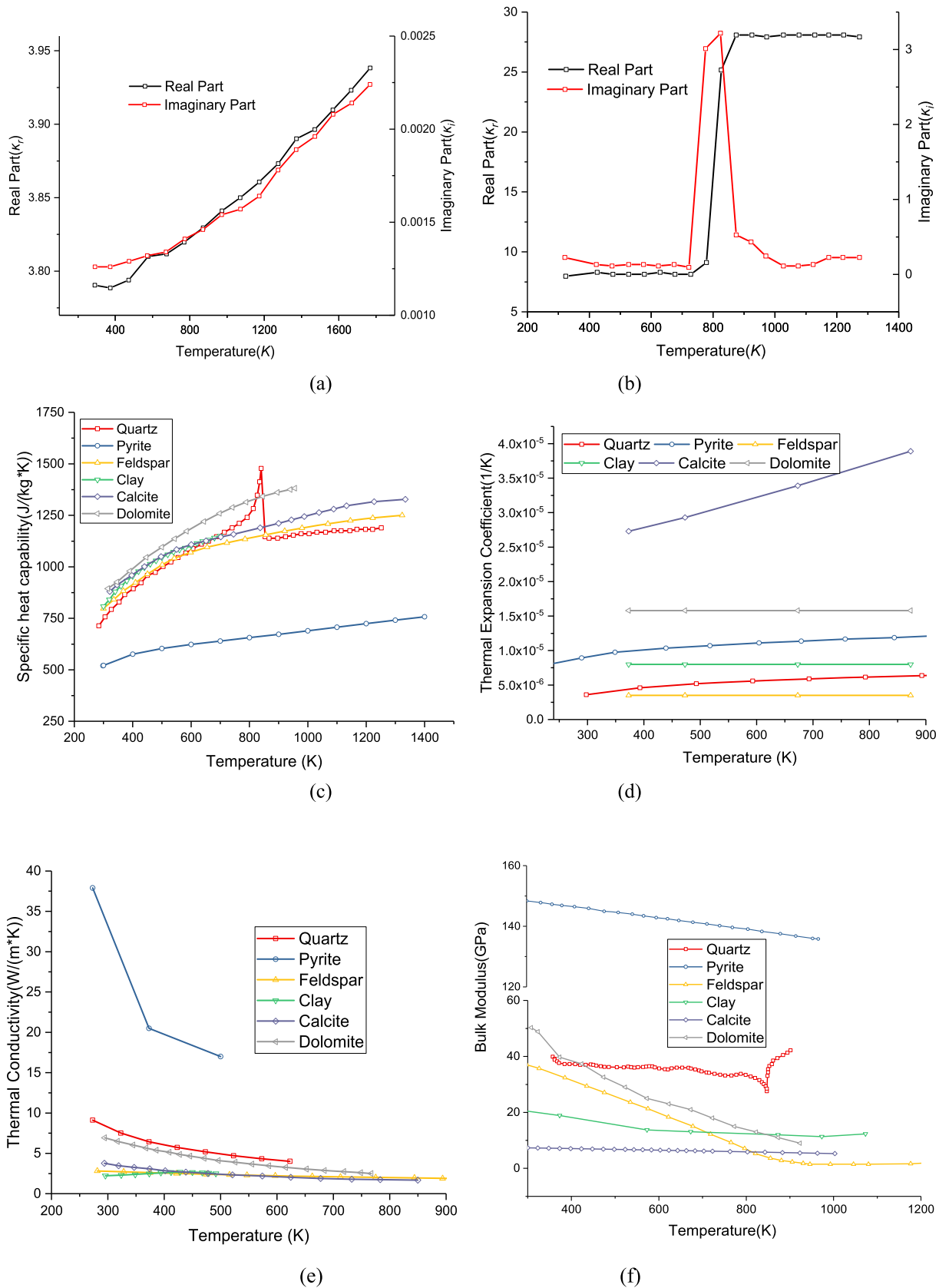
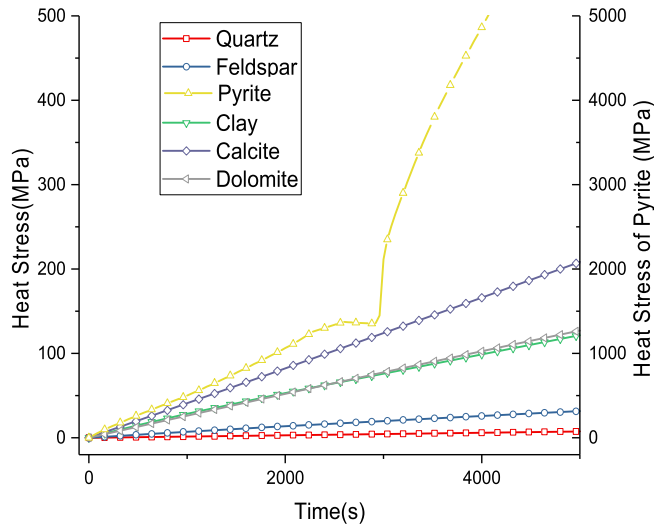


Fig. 9. Relationship of (a) dielectric permittivity of quartz,<sup>51</sup> (b) dielectric permittivity of pyrite,<sup>16</sup> (c) specific heat capacities,<sup>31,52</sup> (d) thermal expansion coefficients,<sup>27,29,53-55</sup> (e) thermal conductivities<sup>53,56-58</sup> and (f) bulk modulus<sup>59,60-64</sup> with temperature for different minerals.

**Table 5**  
Mechanical properties for component minerals comprising the shale matrix.

	Quartz	Feldspar	Pyrite	Clay	Calcite	Dolomite
Poisson ratio <sup>65</sup>	0.08	0.32	0.15	0.35	0.32	0.30
Compressive strength (MPa)	45 <sup>66</sup>	48 <sup>73</sup>	80 <sup>74</sup>	7	48	35 <sup>72</sup>
Tensile strength (MPa)	8.5 <sup>66</sup>	10 <sup>67</sup>	15 <sup>68</sup>	1.5 <sup>69</sup>	10 <sup>71</sup>	5 <sup>72</sup>



**Fig. 10.** Evolution of thermal stress with time of different minerals.

As shown in Fig. 10, the pyrite exhibits the largest heating-induced-stress compared to the other minerals due to its significant permittivity, lower specific heat capacity and largest bulk modulus (see parameters listed in Section 5.1). Also apparent are two stages, due to the sudden increase in permittivity at  $\sim 700$  K as shown in Fig. 9 (b). In addition to the pyrite, the heating stress of the other minerals increases linearly with time in the order of calcite first, followed by dolomite, clay, feldspar, and quartz. The clay minerals endure a smaller heating stress due to their small bulk modulus, even though they have a relatively large dielectric permittivity. Quartz has the lowest heating stress due to its lowest permittivity (Fig. 9 (a)) and largest specific heat capacity (Fig. 9 (c)). Even although its permittivity increases linearly with temperature, it remains in a low range as it is insensitive to temperature increase. These comparisons relate that the ability to convert microwave radiation to thermal stresses is not only related to the microwave propagation and adsorption properties of the mineral (dielectric permittivity,  $\kappa$ ) but is equally dependent on the thermophysical parameters of specific heat capacity, thermal expansion coefficient and deformation modulus. Also, based on Fig. 10, the minerals in the shale matrix can be categorized into the three types – ‘high’, ‘intermediate’ and ‘low’- efficiency in converting microwave energy into thermal stress: For the shale matrix, the ‘high’ conversion efficiency mineral is pyrite, the ‘low’ conversion efficiency minerals are quartz and feldspar with the other minerals belonging to the ‘intermediate’ group.

### 5.3. Mechanical interactions between contrasting minerals

#### 5.3.1. Variations of $\sigma_{1h}$ and impacts of damage

As illustrated in Section 3, the shear stress ( $\tau$ ) along the interface between contrasting minerals and the normal stress ( $\sigma_n$ ) applied on the minerals are closely related to the horizontal stress ( $\sigma_h$ ) as shown in Eqs. (17), (18) and (20). In this section, we investigate the impact of the vertically stacked structure of different minerals on the horizontal stress ( $\sigma_h$ ). The results are shown in Fig. 11.

As aforementioned, the sign convention is tension positive and compression negative. In the subfigures, the characteristics of figures (a)–(f) represent the cases that the mineral  $m_1$  is respectively pyrite, quartz, feldspar, clay, calcite and dolomite; in each figure the horizontal stress (left y-axis) developed in mineral  $m_1$  ( $\sigma_{1h}$ ) with a different mineral  $m_2$  is shown. For example, Fig. 11(a) represents the horizontal stress applied on pyrite when pyrite is combined with other minerals. In the figures, we also report the average temperatures (right y-axis) of the stacked structure and the stress without considering the influence of damage. The different variables are distinguished by the form of the line as: the solid lines with markers represent the stress considering the damage effect; the dotted lines with markers represent the stress with no damage effect considered; the solid lines without markers represent the average temperature for the different cases; the different minerals ( $m_2$ ) are defined by the varied colors.

As shown in the sub-figures, higher temperatures are obtained when minerals of pyrite and clay are combined with other minerals because of the highest dielectric permittivity of pyrite (Fig. 9 (b)) and lowest specific heat capacity of clay (Fig. 9(c)) and when pyrite and clay are combined the highest temperature is obtained. Conversely, lower temperatures are observed for the cases where quartz is combined with other minerals. The lowest temperature is obtained when the quartz and feldspar are combined.

For the induced thermal stress value (the absolute value is used here), the higher values are obtained with combinations of pyrite (‘high’ conversion efficiency) with other minerals as shown in Fig. 11 (a); and lower values result with the combination of feldspar (‘low’ conversion efficiency) with other minerals as shown in Fig. 11 (c). For the stress type, when quartz and feldspar are combined with other minerals, the horizontal stresses applied on quartz and feldspar (both ‘low’ conversion efficiency minerals) are tensile stresses; and for the cases of calcite combined with other minerals, most of the resulting stresses are compressive. In the other combination cases, both compressive and tensile stresses are observed. When damage occurs, the Young’s modulus is decreased according to Eqs. (22) and (23), and the minerals soften as a result, potentially reducing the induced stresses. Based on this characteristic, the occurrence of damage can be obtained where the discrepancies between the two lines appear.

Form the above characteristics, the following conclusions can be drawn. Minerals with high conversion efficiency are readily damaged since the induced horizontal stress ( $\sigma_{1h}$ ) can be large (Fig. 11 (a)) and sufficient to exceed the compressive strength. For minerals with low conversion efficiency, most resulting horizontal stresses are tensile (Fig. 11 (b) and (c)) and the minerals are easily damaged since the tensile strength is significantly smaller than the compressive strength – typically by an order of magnitude.

#### 5.3.2. Variations of $\sigma_{2h}$ and impacts of geometry size

As displayed in Eq. (14), the horizontal stress ( $\sigma_{2h}$ ) is a function of both the restraint coefficient ( $\eta$ ) and the ratio of the areas ( $A_1/A_2$ ).  $A_1/A_2$  represents a geometric effect and can be estimated from the volume fraction of minerals. In this section, the horizontal stress applied to mineral  $m_2$  ( $\sigma_{2h}$ ) is examined and the impacts of the geometric effect are investigated. In the subfigures, the characteristics of figures (a)–(f) represent the case where mineral  $m_1$  is pyrite, quartz, feldspar, clay, calcite and dolomite, respectively; in each sub-figure the horizontal stress applied on mineral  $m_2$  ( $\sigma_{2h}$ ) with the same mineral  $m_1$  is defined. The solid lines with symbols represent the stress considering the geometric effect; and the dotted lines with symbols represent the stress without considering the geometric effect.

When comparing Figs. 11 and 12, we find that the value of  $\sigma_{1h}$ , obtained from the case when mineral A is serving as  $m_1$  and mineral B is serving as  $m_2$ , is equivalent to the value of  $\sigma_{2h}$ , obtained from the case when mineral B is serving as  $m_1$  and mineral A is serving as  $m_2$ . This characteristic confirms the accuracy of the mathematical model. Also, as shown in Fig. 12, the geometric effect exerts little influence when the

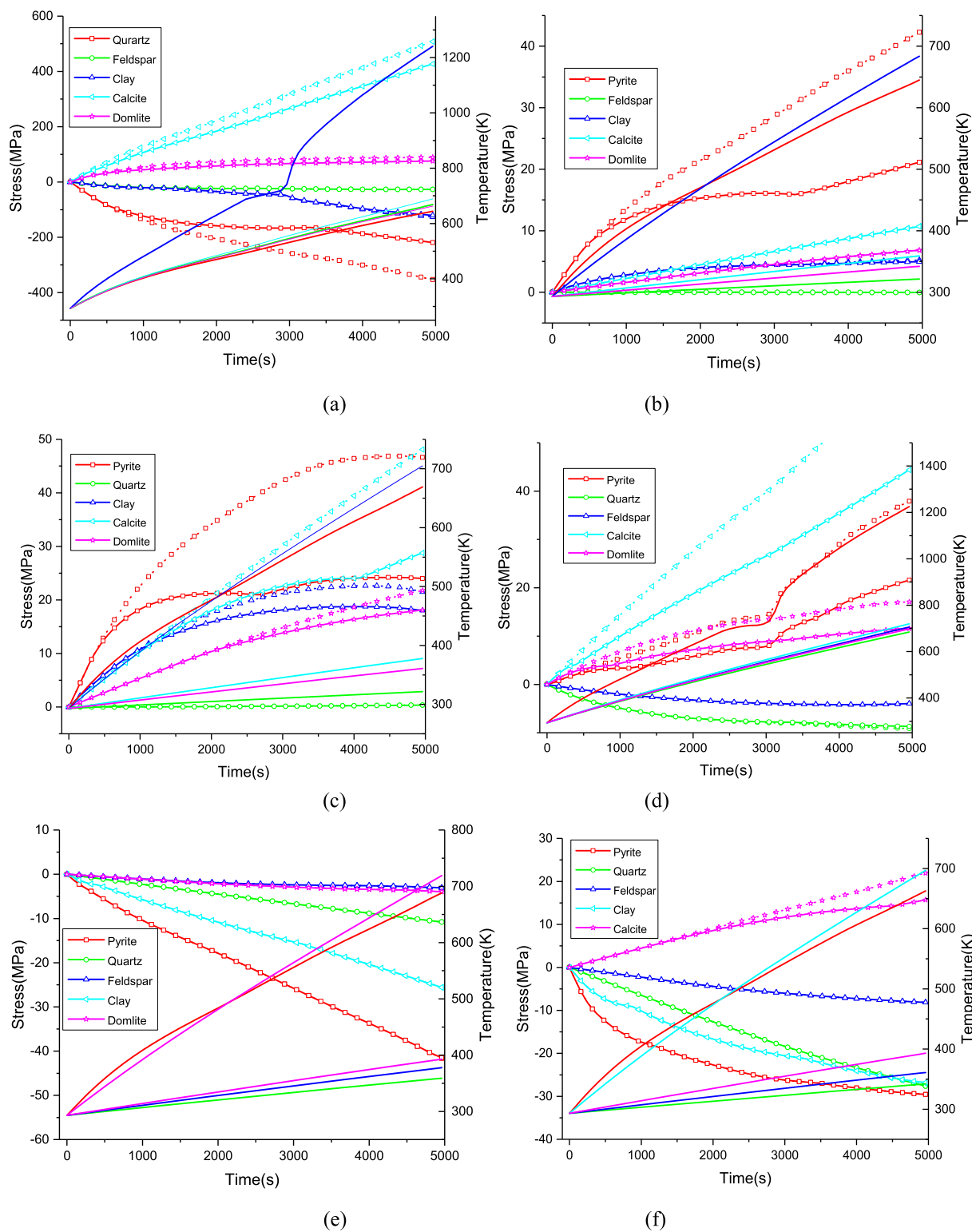


Fig. 11. Variations in horizontal stress applied on mineral  $m_i(\sigma_{1h})$  with (a)~(f) representing cases where mineral  $m_i$  is sequentially (a) pyrite, (b) quartz, (c) feldspar, (d) clay, (e) calcite and (f) dolomite.

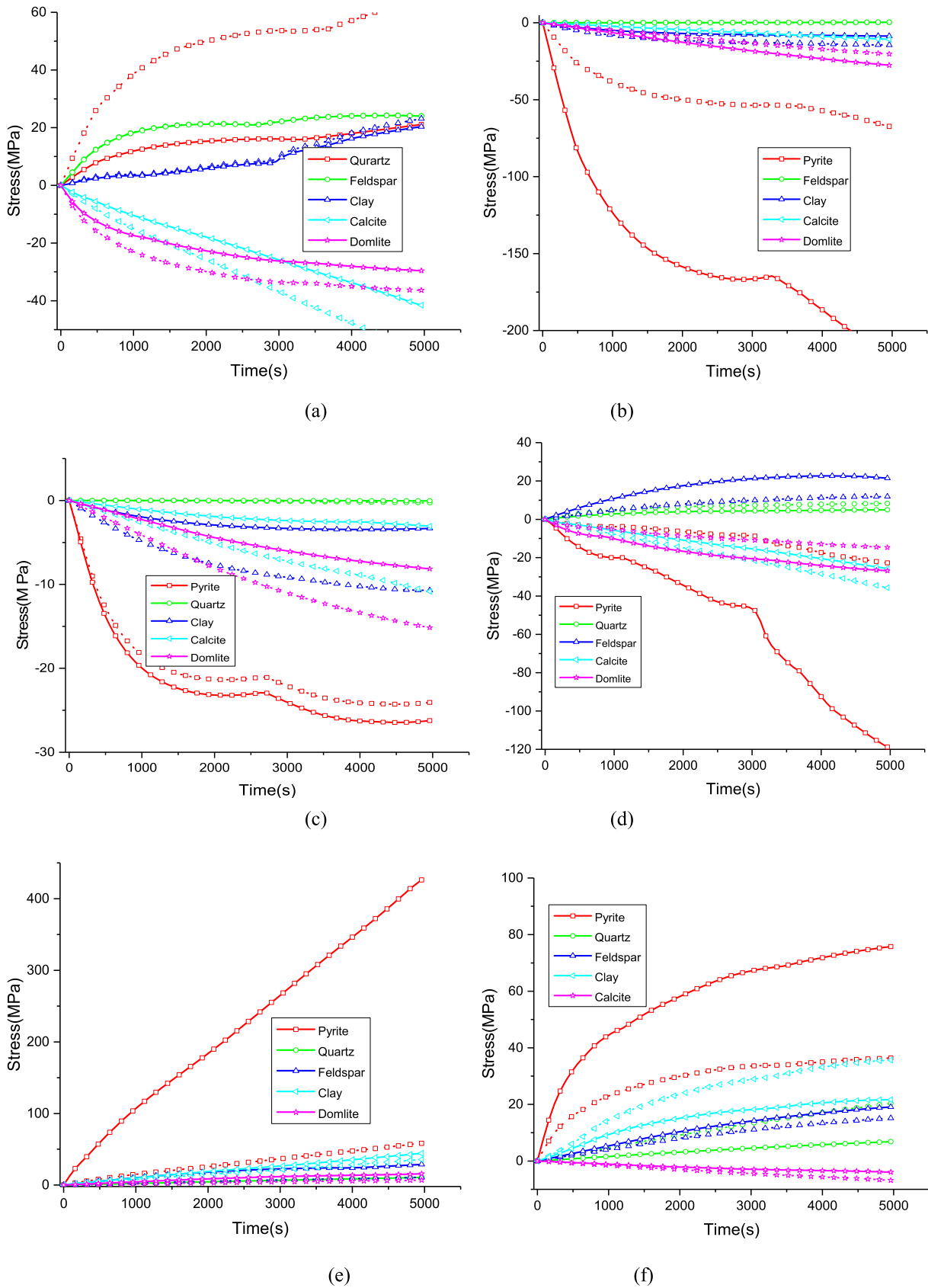


Fig. 12. Variation in horizontal stress applied on mineral  $m_2$  ( $\sigma_{2h}$ ) with (a)~(f) representing cases where mineral  $m_1$  is sequentially (a) pyrite, (b) quartz, (c) feldspar, (d) clay, (e) calcite and (f) dolomite.

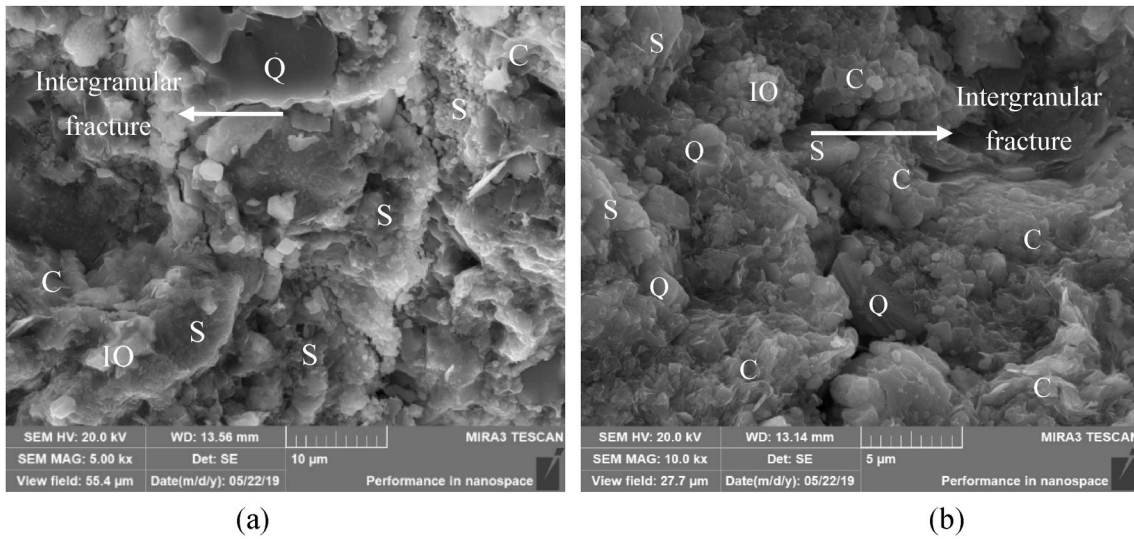


Fig. 13. SEM images of microwave-treated shale matrix to illustrate intergranular fracture. (Q: quartz, F: feldspar, C: clay mineral, IO: Iron oxide, S: sulfate minerals).

volume fractions of the two minerals are close, such as for the combination of feldspar with pyrite, and quartz with calcite as shown in Fig. 12 (a) and (b). Conversely, when the volume ratios of the two minerals are disparate, such as the combinations for pyrite with quartz, and pyrite with calcite, the geometric effect is significant. For the cases when the volume of mineral  $m_1$  is larger than the volume of mineral  $m_2$ , ignoring the geometric effect would over-estimate the horizontal stress applied on mineral  $m_2$  ( $\sigma_{2h}$ ) such as the case when pyrite is combined with other minerals (Fig. 12(a)) and vice versa.

6. Discussions and limitations

6.1. Temperature increasing characteristic of microwave irradiated rock

A three-stage temperature history profile is observed in our simulation work. The temperature first increases rapidly with irradiation time. Above a threshold, the temperature plateaus at constant temperature but increasing irradiation time, due to the phase transition of minerals or evaporation of water; finally, the temperature again increases with

irradiation because of sudden enhancement in dielectric permittivity when the phase transition or the water evaporation process is complete. The three-stage temperature history profile is not proofed in our experiment work because of the short irradiation time. While the similar observations are identified in Pickles’s work<sup>47</sup> in which the nickeliferous limonitic laterite ore was microwave heated. During the first minute, the temperature increased rapidly and then remained constant at about 100 °C for about 3 min because of free water evaporation from the sample. Once this water was removed, then the sample temperature increased very rapidly. Also the three-stage temperature history profile can be found in Liu’s work<sup>46</sup> when the raw coal and absorber (char) were irradiated together. Besides the experiment work, the three increasing stages were also observed in Li’s simulation work.<sup>9</sup>

Also in our work, the impacts of dielectric permittivity on microwave heating process are investigated and found that the enhancement in the imaginary part is the main contribution to the third stage and the real part has a smaller impact. This characteristic is also proofed in Lan’s work.<sup>75</sup> It was found that as the dielectric loss factor (imaginary part) increased, more electromagnetic energy was converted into heat causing

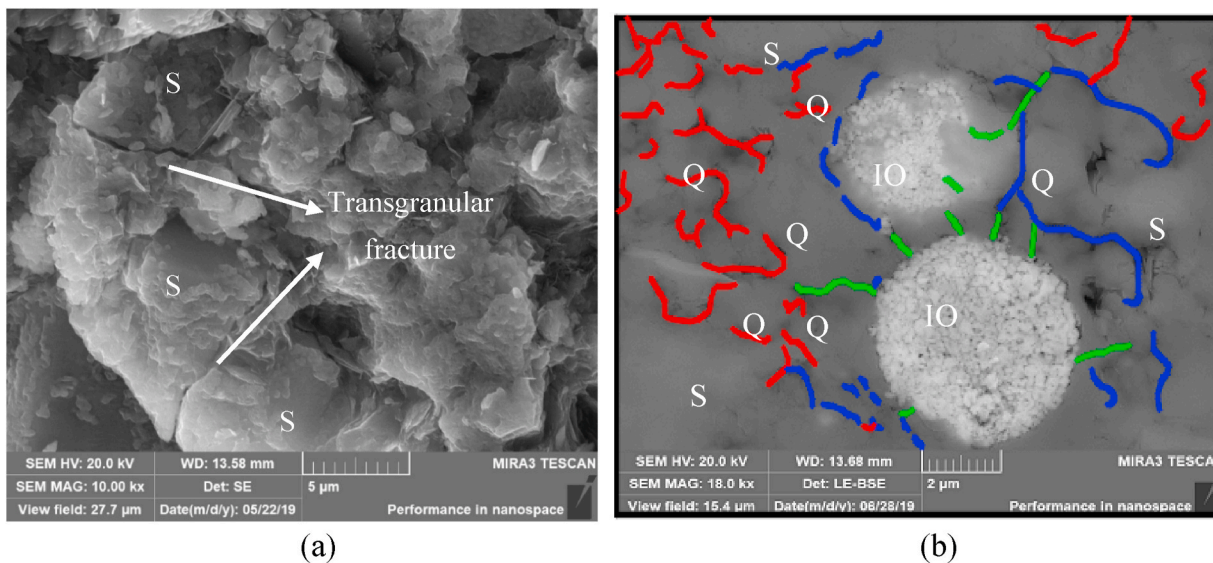


Fig. 14. SEM images of microwave-treated shale matrix to illustrate transgranular fracture. (Q: quartz, F: feldspar, C: clay mineral, IO: Iron oxide, S: sulfate minerals).

coal temperature to increase and the changing real part redistributed the temperature field irregularly. The applicability of our macro-model can also be supported from these observations and characteristics in others works.

## 6.2. Occurrence of intergranular and transgranular fractures

The conditions promoting the evolution of transgranular and intergranular fractures are discussed based on the numerical results displayed in Sections 5.2 and 5.3.

### 6.2.1. Occurrence of intergranular fracture

Intergranular fracture usually occurs along the interface between different minerals caused by the shear stress. As demonstrated in the mathematical model, when two minerals are in welded contact, one mineral will be stretched with the other compressed. This difference applies a resulting shear stress along the interface. Once the shear stress exceeds the maximum yield stress, intergranular fracture will occur. As shown in Eq. (20), the shear stress is related to the magnitude of the horizontal stress ( $\sigma_{1h}$ ) and the aspect ratio ( $l/h_l$ ). A larger horizontal stress ( $\sigma_{1h}$ ) and smaller aspect ratio ( $l/h_l$ ) would result in a larger induced shear stress.

As noted in Section 5.2, the minerals in the shale matrix can be divided into three types based on the conversion efficiency of microwave radiation into thermal stresses. As shown in our results (Fig. 11), a larger induced horizontal stress often occurs in the cases where the difference in the conversion efficiency of the two minerals are large. For the minerals in shale matrix, pyrite has the strongest conversion efficiency compared to other minerals. For other rock types, sulfide minerals and iron-bearing minerals are usually characterized with high conversion efficiencies.<sup>76</sup> Furthermore, they typically comprise only a small volume fraction, exhibiting an irregular polygonal shape and smaller geometric dimensions. Both features would lead to large induced shear stresses.

This conclusion is also supported by observations at micro-scale images obtained from microwave-heated rocks. SEM is applied to characterize the mineral fractures in microwave irradiated shale, with some representative images shown in Fig. 13. In the image, iron oxide and sulfate minerals are produced from pyrite oxidation, which has a strong conversion efficiency of microwave radiation into thermal stresses and a smaller geometric dimension. As observed in the image, intergranular fractures are concentrated around iron oxide and sulfate minerals.<sup>77</sup> In Charikinya et al.<sup>77</sup> work, the intergranular fracture appeared around sphalerite and pyrite which were categorized as high convert ability minerals when the coarse sphalerite ore particles was microwave heated.

### 6.2.2. Occurrence of transgranular fracture

Transgranular fracture occurs within the minerals themselves, instead of along the interface between adjacent and contrasting minerals. There are two factors that induce transgranular fracture when two minerals are combined: (1) One is the horizontal stress ( $\sigma_h$ ), that serves as a compressive stress for the mineral with high conversion efficiency and tensile stress for the mineral with low conversion efficiency. When the stress exceeds the compressive or tensile strength, the minerals will be damaged and the transgranular fracture will appear; (2) The second is the normal stress ( $\sigma_n$ ) serving as the tensile stress for both minerals. The details are discussing in the following.

For horizontal-stress( $\sigma_h$ )-induced transgranular fracture, two types of minerals should be considered: (1) For minerals with high microwave conversion efficiency - horizontal stress is induced as a compressive stress for this kind of mineral. Even if the compressive strength is large, the induced horizontal stress ( $\sigma_h$ ) can readily be large enough to overcome this compressive strength; and (2) For minerals with low microwave conversion efficiency - the horizontal stress may be small but tensile and the minerals are easily damaged since the tensile strength is

much smaller than the compressive strength. For normal stress ( $\sigma_n$ ) induced transgranular fractures, their formation is related to both the horizontal stress ( $\sigma_h$ ) and the aspect ratio ( $h/l$ ) as shown in Eqs. (17) and (18). The latter ratio can be estimated from the volume fraction of the mineral, and the minerals with larger volume fraction would lead to large values of the ratio  $h/l$  and therefore the normal stress. Once the normal stress exceeds the tensile strain, the mineral will be damaged.

The SEM images obtained from our experiments also support this viewpoint. Fig. 14 shows two representative SEM images of microwave-treated shale. Transgranular fracturing is observed in the sulfate minerals produced by pyrite oxidation and characterized with high microwave conversion efficiency (Fig. 14 (a)). In this term, the horizontal stress is compressive and exceeds the compressive strength. In Fig. 14 (b), the transgranular fractures are also found in the quartz which features low microwave conversion efficiency and can be categorized into three types based on their shapes and locations: **Type I**, the fracture direction is perpendicular to the interface with iron oxide featuring high microwave conversion efficiency also defined as radial fractures (green traces). In this case, the transgranular fracture is induced by the horizontal stress which applies a tensile stress. This usually occurs in a low microwave conversion efficiency mineral when it co-exists with a high microwave conversion efficiency mineral; **Type II**, the induced fracture is parallel to the interface, and is referred to as a circular fracture (blue traces). In this term, the transgranular fracture is induced by the normal stress and often occurs in minerals comprising a large volume fraction (high value of  $h/l$ ); **Type III**: the induced transgranular fractures are distant from the high microwave conversion efficiency minerals and are irregularly distributed and in varied directions (red traces). In this case, the fractures may be caused by the high-temperature reaction and decomposition of minerals or water evaporation. The details of mineral reaction- and decomposition-induced fractures are discussed in our recent work<sup>78</sup>.

The similar observations are also found in the work of others. Also in Charikinya et al.<sup>77</sup> work, transgranular fracture is also observed in pyrite, pyrrhotite and sphalerite minerals characterized with high microwave conversion efficiency.<sup>77</sup> This kind of transgranular fracture is caused by the compressive stress induced by the horizontal stress. In Nicco's work,<sup>79</sup> the granodiorite was treated with microwave radiation and most of the transgranular fractures appear in the quartz and feldspar characterized with low microwave conversion efficiency but high volume fraction. Both the circular and radical fractures are observed in these minerals. As discussed above, the radical fractures are induced by the horizontal stress while the circular fractures are induced by the normal stress.

### 6.2.3. Comparisons with numerical and theoretical works

In the above section, the results of the micro-model are verified through the SEM image while the observations and findings of the micro-model are also proofed in other numerical and theoretical works. In this work, the stacked mineral geometries are specified while the similar observations are identified in the previous work in which the nested geometries are assumed. Wang's work<sup>27</sup> accommodated a microwave-adsorbing mineral (pyrite) encased within a low-absorbing matrix mineral (calcite). It was found that (1) the thermal stress were mainly compressive within the pyrite particle and the tensile stress occurred in the calcite; and (2) the tensile stress in calcite increases with the size of pyrite. Also in the Meisels's work,<sup>53</sup> the microwave analysis (finite difference time domain—FDTD) was performed with the absorbing inclusions (discs) embedded in a non-absorbing matrix. The cracks was initiated at the circumference of the discs as well as in the matrix. Most of the cracks were appeared in the radial direction of the discs.

Recently, we develop a nested spherical mechanical model where the heated volume is divided into three zones from inward to outward: an interior high temperature zone (H zone), a transition zone (T zone) and a low temperature external zone (L zone).<sup>80</sup> The microwave heating

induced circumferential stresses are compressive in the innermost region (H zone) but tensile in the transition and exterior (T and L) zones. The location of the initial fracture is most likely located in the L Zone. These observations are also consistent with the findings in this work.

### 6.3. Applications

The potential application of the novel simulation approach proposed in this work are discussed, together with the potential field applications of microwave heating in shale gas reservoir.

#### 6.3.1. Application of simulation approach

In microwave-heating-induced fracturing, the heating process is conducted at the sample scale while the fracturing mechanism is controlled at mineral scale. Therefore a scale mismatch problem results and high meshing quantity is required if the two process are to be simulated with a single model. To compensate for this deficiency, an improved simulation approach is proposed to investigate the electromagnetic-heating-stress-damage process with coupled macroscopic heating linked to microscopic thermal damage. In the macro-model, the microwave heating process is simulated at sample scale. Complementarily, the stress-damage process is simulated at mineral/micro-scale. This simulation approach can also be applied to other physical processes in rock such as gas flow or rock damage processes. The gas flow process into porous rock is taken as an example to illustrate the applications of the novel simulation approach.

Porous rocks typically contain fracture and matrix systems with large differences in the gas storage and transport characteristics and mechanical behavior.<sup>81,82</sup> Mass transport and effective stress transfer between the two systems plays a significant role in the gas flow process.<sup>83</sup> If we investigate at either sample- or reservoir-scale, we typically cannot characterize the geometrical characteristics of the matrix and fracture discretely since the matrix and fracture are usually at millimeter or micrometer scale.<sup>84,85</sup> Therefore, conventionally, dual-porosity models are usually applied.<sup>86</sup> While in such approaches, the mass transport and effective stress transfer between sub-systems are simplified to consider only the gas pressure difference. The novel simulation approach proposed in this work supplies another feasible way to represent interaction between the two systems at different scales and how this interaction affects gas flow behavior. Two types of simulation models should be established: a macro-model in the reservoir or at sample scale and a micro-model representing matrix-fracture interactions at the millimeter or micrometer scale. These two simulation models can be linked or coupled using the following approach: (1) Gas flow in the fracture system is simulated in the macro-model and the gas pressure of a small volume in the sample or reservoir can be obtained; (2) Resulting gas pressures can be transmitted and treated as a fracture pressure in the micro-model; (3) Mass and effective stress transfer processes, and the dependency on fracture permeability evolution is calculated in the micro-model; (4) Updated permeabilities and mass transfer is returned to the first step (Step #1).

#### 6.3.2. Potential field applications

Microwave heating has been studied and applied to unconventional reservoir since the early 1970s.<sup>4</sup> Generally, the RF antenna or induction coil is inserted into the strata heating the reservoir.<sup>12</sup> The microwave heating is usually combined with fracturing methods such as hydrofracturing and causes a series of chemical and mechanic interactions at different scale. (1) At the mineral scale, (i) the organic matter inside the shale matrix can heat up after microwave stimulation and release adsorbed gas;<sup>87</sup> (ii) the microwave irradiation would increase the number of pores therefore enhancing the diffusion in the shale matrix as demonstrated in our recent work.<sup>78</sup> (2) At the micro-scale as proved in this work, (i) shear damage and intergranular fracture usually occurs for minerals with 'high' conversion efficiency form imparting large horizontal stresses; (ii) transgranular fracture can be occur in high

conversion efficiency minerals, due to the induction of a large horizontal stress; and in low conversion efficiency minerals respectively caused by the horizontal stress promoting the radial fracture or by the normal stress inducing circular fracture. (3) At macro-scale, (i) the heating-induced fractures first appear along the bedding then perpendicular to the bedding direction; and (ii) microwave treatment mainly promotes an increase in permeability parallel to the bedding direction; In this work, we paid our attention to the micro-scale and the impact of the microwave irradiation on the shale permeability (macro-scale) are described in our recent work.<sup>78</sup>

Prior the microwave heating, the hydraulic fracture is the essential step to the exploration of shale reservoir due to its ultra-low permeability. While a large fraction of injected fracturing fluid cannot be recovered and remain in the fracture imbibing into the shale matrix. Additionally, shale gas reservoirs usually contain a certain amount of connate water which is subdivided into free water and irreducible water.<sup>88</sup> The presence of water would swell the clay impairing the intrinsic permeability and reduce the gas relative permeability because of the occupation of water molecular. After the microwave irradiation, the retained water is evaporated and both the intrinsic and gas relative permeabilities are improved.<sup>89</sup> Besides this, the saturated vapor pressure would be larger than the tensile strength of shale matrix causing the local failure therefore inducing fracture and increasing intrinsic permeability.<sup>90</sup> While the literature also suggested that the new fractures are hardly generated when the moisture reaches a threshold.<sup>91</sup> Therefore an optimal moisture content exist to achieve the best microwave heating effect.

For the reservoir application, the penetration depth ( $D_p$ ) should be considered as microwave penetrates into a material, its amplitude diminishes.  $D_p$  is written as:<sup>10</sup>

$$D_p = \frac{C}{2\pi f \sqrt{2\kappa_r} \left( \sqrt{1 + \tan^2 \left( \frac{\kappa_i}{\kappa_r} \right)} - 1 \right)^{1/2}} \quad (26)$$

where  $C$  is the speed of light, m/s;  $f$  is the frequency, Hz;  $D_p$  in shale is on a scale of meters<sup>10</sup> constraining the application of the microwave heating. As indicated in Eq. (26), reducing frequency is common approach to achieve a larger effective heating range while the lower frequency microwaves carry less energy with long irradiation time needed to obtain the same heating effect.

### 6.4. Limitations

Rock is a highly heterogeneous material and, in addition to minerals, also contains cracks, grain boundary weaknesses and cleavage, which are not incorporated into the current model. In addition, true and rigorous verification of the micro-model is difficult since the heating stresses are never measured at the mineral scale. Furthermore the impacts of the water evaporation are not considered in this work. Therefore it is suitable to discuss the assumptions and limitations of this work.

#### 6.4.1. Mineral phase transition and decompositions

The conversion efficiency of microwave radiation into differential thermal stresses is related to the electromagnetic, thermodynamic and mechanical parameters with strong temperature dependences displayed in Section 5.1. Thus, special attention should be paid to the presence of quartz since quartz exhibits an  $\alpha$ - $\beta$  transition at 573 °C.<sup>45</sup> This phase transition is accompanied by a change in symmetry and volume. Clearly, the sudden change in the specific heat capacity and Young's modulus in quartz-rich rock are induced by this phase transition.<sup>45</sup> Also the  $C_p$ - $T$  curve used in this work contains a distinct peak and its impacts on the microwave heating process are investigated in Section 4.2. In shale, the nanometer-sized pores are mainly inside the organic matter – and this heats rapidly under microwave irradiation. When the temperature is above 400 °C, oxidation of organic matter begins to occur<sup>92</sup> releasing

carbon dioxide<sup>93</sup> and being responsible for the development of pores in the organic matter. Calcite in the shale can also decompose into calcium oxide and carbon dioxide at high temperature<sup>15</sup> responsible for the formation of pores in calcite minerals.

The parameters used in this study are temperature-dependent and their applicability and limitations should be considered. (i) In the macro model, the dielectric permittivity-temperature curve and specific heat capacity-temperature curve are assumed to fit the experimental data - the impacts of their temperature dependences are also investigated. This influence may have some effect on the evolution of temperature but will have little effect on the pattern of variation and conclusions; (ii) In the micro-model, the parameters of different minerals are collected from the literature with the impacts of the phase transition of quartz considered. First, these parameters are collected from the other rocks instead of shale; and second, the phase transition and reaction processes of other minerals are not considered. Taking clay as an example, for temperatures in the range  $125\text{ }^{\circ}\text{C} < T < 250\text{ }^{\circ}\text{C}$ , the hydrosopic water in illite is lost; when the temperature transits from  $350\text{ }^{\circ}\text{C}$  to  $550\text{ }^{\circ}\text{C}$ , the structure of illite transforms to mica and this might impact the conclusions of this study; (iii) The mechanical properties of the minerals are considered independent of strain rates which may be a simplification since the stiffness properties of the material may change at extremely high strain rates due to rapid heating; (iv) some parameter-temperature relationships are not available since they are difficult to determine such as the dielectric permittivities.

#### 6.4.2. Applicability of assumptions

In this work, several assumptions are made during the simulation process and in the mathematical model. The feasibility and applicability of these assumptions may be questioned, item by item. (i) The electric field ( $E_e$ ) of a small volume of the sample was selected as a medium linking the macro- and micro-models. The heating processes on the different minerals are calculated through Eq. (9), assuming a uniform electric field ( $E_e$ ) but with different imaginary parts of dielectric permittivity – the impacts of the real part are ignored. This process leads to a contradiction that an induced temperature magnitude can be obtained from the small volume of the shale sample but the temperature values vary with different minerals at the micro-scale in the same area. In fact, the temperature obtained from the sample is a macroscopic representation of the mineral temperatures at the micro-scale. Also, a similar phenomenon is observed in the mechanical parameters. The rock has a Young's modulus at the macro scale but the values for different minerals are varied at the micro scale as observed under AFM (Atomic Force Microscope);<sup>94</sup> (ii) In the establishment of the mathematical model, it is assumed that no relative slippage occurs between the two minerals – that they are fully welded together. It should be noted that this assumption is only available in the elastic range. When the two minerals are damaged by the horizontal stresses ( $\sigma_h$ ) or the shear stress ( $\tau$ ), then fractures will be generated and relative-slip may result between the different minerals. Fracture generation and subsequent interface-slip processes are not simulated in the current work. Instead, the stress-strain relationship following mineral damage is described by a power function and the related parameters are specified artificially since they are difficult to measure at mineral scale. The maximum compressive stress criterion is used instead of the Mohr-Coulomb criterion for simplicity; (iii) Unstressed samples are used in the modeling and fracturing evaluated. The application of a confining stress will inhibit fracture formation, but this impact can intrinsically be evaluated using the same approaches developed here. This is the topic of future exploration.

#### 6.4.3. Water evaporation

As mentioned above, both the injected water and native formation water exist in the simulated shale reservoir. The related literature suggested that the thermodynamic (specific heat capacity,  $C_p$ ) and electromagnetic parameters (dielectric permittivity,  $\kappa$ ) are strongly water saturation-dependent.<sup>95,96</sup> After microwave irradiation, the free water is

quickly evaporated while more temperature and energies are needed to remove the connate water.<sup>97</sup> The adsorbed and interlay water would be excluded at least  $100\text{--}200\text{ }^{\circ}\text{C}$  while  $400\text{ }^{\circ}\text{C}$  is necessary to remove constitution water in the lattice.<sup>97</sup> During these processes, all the adsorbed energy is converted to the internal energy forcing water to evaporate. As a result, the temperature would keep as a constant value with the irradiation time leading to a peak in the specific heat capacity-temperature curve ( $C_p$ - $T$ ). In the macro-model verification process, we established a  $C_p$ - $T$  curve and its peak value is much higher than that caused by the phase transition and the peak range is also much wider. This is mainly because of water evaporation.

Water is also a high microwave adsorption medium with the imaginary part value of 12 at  $25\text{ }^{\circ}\text{C}$  and 2.45 GHz. Even the value decreases with temperature (3 at  $85\text{ }^{\circ}\text{C}$  and 2.45 GHz), it is still much higher than that of shale matrix. After microwave irritation, water is firstly activated and gradually driven off the shale matrix. As a result, both real and imaginary permittivity values suffer a reduction before 800 K as shown in Fig. 5(a). While in this work only the retained water is considered and the impact of water is not significant compared with other works.<sup>95,96</sup>

## 7. Conclusions

Previous work representing microwave heating and damage has been principally uncoupled between processes (irradiation-heating-fracture), has not transited multiple scales (macro-sample to micro-mineral), and has considered nested mineral geometries that are not consistent with nature. To compensate for these deficiencies, a coupled macro-scale irradiation/heating model is linked to a corresponding micro-scale mechanical/damage model to simulate the microwave heating process on the sample and the resulting heating induced damage to the mineral aggregate. Through above work, the following conclusions are obtained:

- (1) The macro-model accommodates the microwave heating process at sample scale, enabling the impacts of temperature-dependent parameters to be investigated. A three-stage temperature history profile is observed in shale that is broadly applicable to other rocks: linearly increase stage due to the low value of  $C_p$ , plateau stage due to the minerals phase transition or water evaporation, and sudden increase stage because of enhancement in dielectric permittivity. These three periods are apparent for the specific sample of shale, but may not all appear for all rock, depending on their thermodynamic composition.
- (2) A mathematical model is established to evaluate the evolution of stress state at micro-scale. The model accommodates the evolution of stress in three forms: horizontal stress ( $\sigma_h$ ) and the normal stress ( $\sigma_n$ ) applied on the minerals, and the shear stress ( $\tau$ ) applied on the interface between different minerals. Evolution of these stresses are related in a complex manner to contrasting magnitudes of electromagnetic, thermodynamic and mechanical properties together with idealized characteristic geometric dimensions of the aggregate.
- (3) The heating stress induced damage process is examined at the mineral scale. The minerals comprising the shale matrix are categorized into three types – 'high', 'intermediate' and 'low' – conversion efficiency based on their susceptibility to thermal stressing from microwave irradiation, representing various combinations of microwave adsorption and thermophysical characteristics. The influence of mineral size is small when the volume fractions of the two minerals are similar and vice versa.
- (4) Conditions promoting the preferred appearance of either intergranular or transgranular fracture are defined. Shear damage and intergranular fracture usually occurs for minerals with 'high' conversion efficiency imparting large horizontal stresses and characterized with a small volumetric proportion and an irregular polygonal form; The conditions promoting the appearance of

transgranular fracture is complex: in high conversion efficiency minerals, due to the induction of a large horizontal stress ( $\sigma_h$ ) serving as the compressive stress; and in low conversion efficiency minerals respectively caused by the horizontal stress ( $\sigma_h$ ) promoting the radial fracture or by the normal stress ( $\sigma_n$ ) inducing circular fracture.

- (5) The simulation approach proposed in this work provides a powerful way to link the macro-scale characterization and heating to micro-mechanisms of rock failure. This simulation approach can also be applied to other physical processes in rock such as gas flow or rock damage processes. Also this work provides mineral classification and criteria to define a priori evaluation of the effectiveness of microwave treatment of shales and other mineral aggregates.

#### Declaration of competing interest

The authors declare that they have no known competing financial interests or personal relationships that could have appeared to influence the work reported in this paper.

#### Acknowledgments

The research delivered partial results under supports of China Postdoctoral Science Foundation, China (2019M661118), the Fundamental Research Funds for the Central Universities, China (No. 02070022119023) and the 111 Project, China (B17009).

#### Appendix A. Supplementary data

Supplementary data to this article can be found online at <https://doi.org/10.1016/j.ijrmms.2020.104520>.

#### References

- Tan Y, Pan Z, Liu J, et al. Experimental study of impact of anisotropy and heterogeneity on gas flow in coal. Part I: diffusion and adsorption. *Fuel*. 2018;232:444–453.
- Yan Q, Lemanski C, Karpyn ZT, Ayala L. Experimental investigation of shale gas production impairment due to fracturing fluid migration during shut-in time. *J Nat Gas Sci Eng*. 2015;24:99–105.
- Chakraborty N, Karpyn ZT. Gas permeability evolution with soaking time in ultra tight shales. In: *SPE Annual Technical Conference and Exhibition*. Society of Petroleum Engineers; 2015.
- Bera A, Babadaghi T. Status of electromagnetic heating for enhanced heavy oil/bitumen recovery and future prospects: a review. *Appl Energy*. 2015;151:206–226.
- Sadeghi A, Hassanzadeh H, Harding TG. A comparative study of oil sands preheating using electromagnetic waves, electrical heaters and steam circulation. *Int J Heat Mass Tran*. 2017;111:908–916.
- Bientinesi M, Petarca L, Cerutti A, et al. A radiofrequency/microwave heating method for thermal heavy oil recovery based on a novel tight-shell conceptual design. *J Petrol Sci Eng*. 2013;107:18–30.
- Folorunso O, Dodds C, Dimitrakis G, Kingman S. Continuous energy efficient exfoliation of vermiculite through microwave heating. *Int J Miner Process*. 2012;114:69–79.
- Somani A, Nandi TK, Pal SK, Majumder AK. Pre-treatment of rocks prior to comminution—a critical review of present practices. *Int J Min Sci Technol*. 2017;27(2):339–348.
- Li H, Shi S, Lin B, et al. A fully coupled electromagnetic, heat transfer and multiphase porous media model for microwave heating of coal. *Fuel Process Technol*. 2019;189:49–61.
- Liu J, Wang J, Leung C, Gao F. A fully coupled numerical model for microwave heating enhanced shale gas recovery. *Energies*. 2018;11(6):1608.
- Wei W, Shao Z, Zhang Y, Qiao R, Gao J. Fundamentals and applications of microwave energy in rock and concrete processing – a review. *Appl Therm Eng*. 2019;157:113751.
- Huang J, Xu G, Liang Y, Hu G, Chang P. Improving coal permeability using microwave heating technology—a review. *Fuel*. 2020;266:117022.
- Jones DA, Kingman SW, Whittles DN, Lowndes IS. The influence of microwave energy delivery method on strength reduction in ore samples. *Chem Eng Process*. 2007;46(4):291–299.
- Nicco M, Holley EA, Hartlieb P, Pfaff K. Textural and mineralogical controls on microwave-induced cracking in granites. *Rock Mech Rock Eng*. 2020;53:4745–4765.
- Wang H, Rezaee R, Saeedi A. Preliminary study of improving reservoir quality of tight gas sands in the near wellbore region by microwave heating. *J Nat Gas Sci Eng*. 2016;32:395–406.
- Lovás M, Kováčová M, Dimitrakis G, Čuvanová S, Znamenáčková I, Jakabský Š. Modeling of microwave heating of andesite and minerals. *Int J Heat Mass Tran*. 2010;53(17–18):3387–3393.
- Zheng Y, Wang S, Feng J, Ouyang Z, Li X. Measurement of the complex permittivity of dry rocks and minerals: application of polythene dilution method and Lichtenecker's mixture formulae. *Geophys J Int*. 2005;163(3):1195–1202.
- Church RH, Webb WE, Salsman J. *Dielectric Properties of Low-Loss Minerals*. Institution of Engineering and Technology; 1988.
- Ali AY, Bradshaw SM. Quantifying damage around grain boundaries in microwave treated ores. *Chem Eng Process*. 2009;48(11):1566–1573.
- Hassani F, Nekoovaght PM, Gharib N. The influence of microwave irradiation on rocks for microwave-assisted underground excavation. *J Rock Mech Geotech*. 2016;8(1):1–15.
- Wang Y, Forssberg E. Dry comminution and liberation with microwave assistance. *Scand J Metall*. 2005;34(1):57–63.
- Metaxas AA, Meredith RJ. *Industrial Microwave Heating*. Institution of Engineering and Technology; 1983.
- Whittles D, Kingman S, Reddish D. Application of numerical modelling for prediction of the influence of power density on microwave-assisted breakage. *Int J Miner Process*. 2003;68(1–4):71–91.
- Jones D, Kingman S, Whittles D, Lowndes I. The influence of microwave energy delivery method on strength reduction in ore samples. *Chem Eng Process*. 2007;46(4):291–299.
- Jones DA, Kingman S, Whittles D, Lowndes I. Understanding microwave assisted breakage. *Min Eng*. 2005;18(7):659–669.
- Meisels R, Toifl M, Hartlieb P, Kuchar F, Antretter T. Microwave propagation and absorption and its thermo-mechanical consequences in heterogeneous rocks. *Int J Miner Process*. 2015;135:40–51.
- Wang Y, Djordjevic N. Thermal stress fem analysis of rock with microwave energy. *Int J Miner Process*. 2014;130:74–81.
- Li J, Kaunda RB, Arora S, Hartlieb P, Nelson PP. Fully-coupled simulations of thermally-induced cracking in pegmatite due to microwave irradiation. *J Rock Mech Geotech*. 2019;11(2):242–250.
- Toifl M, Meisels R, Hartlieb P, Kuchar F, Antretter T. 3d numerical study on microwave induced stresses in inhomogeneous hard rocks. *Min Eng*. 2016;90:29–42.
- Wang H, Rezaee R, Saeedi A, Josh M. Numerical modelling of microwave heating treatment for tight gas sand reservoirs. *J Petrol Sci Eng*. 2017;152:495–504.
- Toifl M, Hartlieb P, Meisels R, Antretter T, Kuchar F. Numerical study of the influence of irradiation parameters on the microwave-induced stresses in granite. *Min Eng*. 2017;103–104:78–92.
- Pitchai K, Chen J, Birla S, Gonzalez R, Jones D, Subbiah J. A microwave heat transfer model for a rotating multi-component meal in a domestic oven: development and validation. *J Food Eng*. 2014;128:60–71.
- Zhang XG, Ranjith PG, Perera MSA, Ranathunga AS, Haque A. Gas transportation and enhanced coalbed methane recovery processes in deep coal seams: a review. *Energy Fuel*. 2016;30(11):8832–8849.
- Jiajia C, Krishnamoorthy P, Sohan B, Mehrdad N, David J, Jayamkondan S. Heat and mass transport during microwave heating of mashed potato in domestic oven-model development, validation, and sensitivity analysis. *J Food Sci*. 2015;79(10):E1991–E2004.
- Chen T, Feng X-T, Pan Z. Experimental study of swelling of organic rich shale in methane. *Int J Coal Geol*. 2015;150–151:64–73.
- Saif T, Lin Q, Butcher AR, Bijeljic B, Blunt MJ. Multi-scale multi-dimensional microstructure imaging of oil shale pyrolysis using X-ray micro-tomography, automated ultra-high resolution sem, maps mineralogy and fib-sem. *Appl Energy*. 2017;202:628–647.
- Zhu WC, Wei CH. Numerical simulation on mining-induced water intrusions related to geologic structures using a damage-based hydromechanical model. *Environ Earth Sci*. 2010;62(1):43–54.
- Wang J, Elsworth D, Wu Y, Liu J, Zhu W, Liu Y. The influence of fracturing fluids on fracturing processes: a comparison between water, oil and SC-CO<sub>2</sub>. *Rock Mech Rock Eng*. 2018;51:299–313.
- Cui G, Wei J, Feng X-T, et al. Preliminary study on the feasibility of co-exploitation of coal and uranium. *Int J Rock Mech Min Sci*. 2019;123:104098.
- Zhou J, Wei J, Yang T, Zhu W, Li L, Zhang P. Damage analysis of rock mass coupling joints, water and microseismicity. *Tunn Undergr Space Technol*. 2018;71:366–381.
- Multiphysics COMSOL. *Help document*. COMSOL; 2018. Version 5.4.
- Multiphysics COMSOL. *Application libraries*. COMSOL; 2018. Version 5.4.
- Al-Harashsheh M, Kingman S, Saeid A, Robinson J, Dimitrakis G, Alnawafleh H. Dielectric properties of Jordanian oil shales. *Fuel Process Technol*. 2009;90(10):1259–1264.
- Rajeshwar K, Inguva R. Application of dielectric spectroscopy to chemical characterization of oil shales. *Fuel*. 1985;64(7):931–937.
- Hartlieb P, Toifl M, Kuchar F, Meisels R, Antretter T. Thermo-physical properties of selected hard rocks and their relation to microwave-assisted comminution. *Min Eng*. 2016;91:34–41.
- Liu H-P, Chen T-P, Li Y, Song Z-Y, Wang S-W, Wu S-H. Temperature rise characteristics of zhundong coal during microwave pyrolysis. *Fuel Process Technol*. 2016;148:317–323.
- Pickles CA. Microwave heating behaviour of nickeliferous limonitic laterite ores. *Min Eng*. 2004;17(6):775–784.

- 48 Cui G, Tan Y, Yu H, et al. An effective dual-medium approach to simulate microwave heating in strongly heterogeneous rocks. *Appl Therm Eng.* 2020. submitted for publication.
- 49 Josh M, Clennell B. Broadband electrical properties of clays and shales: comparative investigations of remolded and preserved samples broadband electrical properties of clay. *Geophysics.* 2015;80(2):D129–D143.
- 50 Aqil S, Schmitt DR. *Dielectric Permittivity of Clay Adsorbed Water: Effect of Salinity.* GeoConvention; 2010:1–4.
- 51 Zhou Y, Li E, Guo G, Gao Y, Yang T. Broadband complex permittivity measurement of low loss materials over large temperature ranges by stripline resonator cavity using segmentation calculation method. *Prog Electromagn Res.* 2011;113:143–160.
- 52 Skauge A, Fuller N, Hepler LG. Specific heats of clay minerals: sodium and calcium kaolinites, sodium and calcium montmorillonites, illite, and attapulgite. *Thermochim Acta.* 1983;61(1):139–145.
- 53 Meisels R, Toifl M, Hartlieb P, Kuchar F, Antretter T. Microwave propagation and absorption and its thermo-mechanical consequences in heterogeneous rocks. *Int J Miner Process.* 2015;135:40–51.
- 54 Luque A, Leiss B, Álvarez-Lloret P, et al. Potential thermal expansion of calcitic and dolomitic marbles from andalusia (Spain). *J Appl Crystallogr.* 2011;44(6):1227–1237.
- 55 Wang X, Shao H, Hesser J, Zhang C, Wang W, Kolditz O. Numerical analysis of thermal impact on hydro-mechanical properties of clay. *J Rock Mech Geotech.* 2014;6(5):405–416.
- 56 Gail HP, Trieloff M. Thermal evolution and sintering of chondritic planetesimals iv. Temperature dependence of heat conductivity of asteroids and meteorites. *Astron Astrophys.* 2018;615:A147.
- 57 Merriman JD, Hofmeister AM, Roy DJ, Whittington AG. Temperature-dependent thermal transport properties of carbonate minerals and rocks. *Geosphere.* 2018;14(4):1961–1987.
- 58 Ghahremannejad B. *Thermo-mechanical Behaviour of Two Reconstituted Clays.* Ph.D. thesis. Australia: University of Sydney; 2003.
- 59 Peng Z, Redfern SAT. Mechanical properties of quartz at the  $\alpha$ - $\beta$  phase transition: implications for tectonic and seismic anomalies. *G-cubed.* 2013;14(1):18–28.
- 60 Wen X, Liang Y, Bai P, et al. First-principles calculations of the structural, elastic and thermodynamic properties of mackinawite (FeS) and pyrite (FeS<sub>2</sub>). *Physica B.* 2017; 525:119–126.
- 61 Chen Y-L, Wang S-R, Ni J, Azzam R, Fernández-steeger TM. An experimental study of the mechanical properties of granite after high temperature exposure based on mineral characteristics. *Eng Geol.* 2017;220:234–242.
- 62 Dandekar DP, Ruoff AL. Temperature dependence of the elastic constants of calcite between 160° to 300°K. *J Appl Phys.* 1968;39(13):6004–6009.
- 63 Ahmed MF, Waqas U, Arshad M, Rogers JD. Effect of heat treatment on dynamic properties of selected rock types taken from the salt range in Pakistan. *Arab J Geosci.* 2018;11(22):728.
- 64 Sun Q, Zhang W, Qian H. Effects of high temperature thermal treatment on the physical properties of clay. *Environ Earth Sci.* 2016;75(7):610.
- 65 Mavko G, Mukerji T, Dvorkin J. *The Rock Physics Handbook: Tools for Seismic Analysis of Porous Media.* 2 ed. Cambridge: Cambridge University Press; 2009.
- 66 Rovnanik P. Effect of the aggregate type on the properties of alkali-activated slag subjected to high temperatures. *Mater Tehnol.* 2015;49(5):709–713.
- 67 Mahabadi OK, Lisjak A, Munjiza A, Grasselli G, Y-geo. New combined finite-discrete element numerical code for geomechanical applications. *Int J GeoMech.* 2012;12(6): 676–688.
- 68 Charikinya E, Bradshaw S, Akdogan G. Effects of model resolution on bonded particle modelling of microwave induced cracks in sulphide ore particles. In: *9th South African Conference on Computational and Applied Mechanics.* Somerset West; 2014.
- 69 Elhamedouni Y, Khabbazi A, Benayad C, Mounir S, Dadi A. Thermophysical and mechanical characterization of clay bricks reinforced by alfa or straw fibers. *IOP Conf Ser Mater Sci Eng.* 2017;186, 012035.
- 70 Buchwald A, Dominowski K, Weil M. The influence of calcium content on the performance of geopolymeric binder especially the resistance against acids. In: *4th International Conference on Geopolymers.* 2005.
- 71 Jones DA, Kingman SW, Whittles DN, Lowndes IS. Understanding microwave assisted breakage. *Min Eng.* 2005;18(7):659–669.
- 72 Sallam HEM, Saba AM, Khalil HS, El-Din HS. Mechanical properties of hybrid coarse aggregate concrete. In: *Al-Azhar Engineering Eighth International Conference.* 2004.
- 73 Tateyama H, Jinnai K, Kimura K, Tsunematsu K. Variation of compressive strength of quartz, feldspar particles in granite by weathering. *J Clay Sci Soc Jpn.* 1980;20(4): 129–133.
- 74 Barratt DJ. Pebble crushing circuit design. In: *SME Annual Meeting and Exhibit.* 1992.
- 75 Lan W, Wang H, Zhang X, et al. Investigation on the mechanism of micro-cracks generated by microwave heating in coal and rock. *Energy.* 2020;206:118211.
- 76 Lu G-m, Li Y-h, Hassani F, Zhang X. The influence of microwave irradiation on thermal properties of main rock-forming minerals. *Appl Therm Eng.* 2017;112: 1523–1532.
- 77 Charikinya E, Bradshaw S, Becker M. Characterising and quantifying microwave induced damage in coarse sphalerite ore particles. *Min Eng.* 2015;82:14–24.
- 78 Chen T, Zheng X, Qiu X, et al. Experiment study on the feasibility of microwave stimulation for enhanced shale gas recovery. *J Nat Gas Sci Eng.* 2020. submitted for publication.
- 79 Nicco M, Holley EA, Hartlieb P, Kaunda R, Nelson PP. Methods for characterizing cracks induced in rock. *Rock Mech Rock Eng.* 2018;51(7):2075–2093.
- 80 Yu H, Li Y, Cui G, Elsworth D, Liu J, Liu M. A model for focused-beam microwave heating on rock fracturing. *Int J Rock Mech Min Sci.* 2020. submitted for publication.
- 81 Cui G, Xia-Ting F, Pan Z, et al. Impact of shale matrix mechanical interactions on gas transport during production. *J Petrol Sci Eng.* 2020;184:106524.
- 82 Cui G, Liu J, Wei M, Shi R, Elsworth D. Why shale permeability changes under variable effective stresses: new insights. *Fuel.* 2018;213:55–71.
- 83 Cui G, Liu J, Wei M, Feng X, Elsworth D. Evolution of permeability during the process of shale gas extraction. *J Nat Gas Sci Eng.* 2018;49:94–109.
- 84 Wang L, Chen Z, Wang C, Elsworth D, Liu W. Reassessment of coal permeability evolution using steady-state flow methods: the role of flow regime transition. *Int J Coal Geol.* 2019;211:103210.
- 85 Chen T, Feng X-T, Cui G, Tan Y, Pan Z. Experimental study of permeability change of organic-rich gas shales under high effective stress. *J Nat Gas Sci Eng.* 2019;64:1–14.
- 86 Warren JE, Root PJ. The behavior of naturally fractured reservoirs. *SPE J.* 1963;3(3): 245–255.
- 87 Arunachalam K, Fan X. Impact of heat of sorption on thermal enhanced recovery of sorbed gas from gas shale reservoirs – an experimental and simulation study. *J Nat Gas Sci Eng.* 2020;79:103318.
- 88 Cheng P, Tian H, Xiao X, Gai H, Li T, Wang X. Water distribution in overmature organic-rich shales: implications from water adsorption experiments. *Energy Fuel.* 2017;31(12):13120–13132.
- 89 Liu J, Liang X, Xue Y, Yao K, Fu Y. Numerical evaluation on multiphase flow and heat transfer during thermal stimulation enhanced shale gas recovery. *Appl Therm Eng.* 2020;178:115554.
- 90 Chen J, Althaus S, Liu H, et al. Electromagnetic-heating enhancement of source rock permeability for high recovery. *Fuel.* 2021;283:118976.
- 91 Huang J, Hu G, Xu G, Nie B, Yang N, Xu J. The development of microstructure of coal by microwave irradiation stimulation. *J Nat Gas Sci Eng.* 2019;66:86–95.
- 92 Han X, Liu Q, Jiang X. Heat transfer characteristic of oil shale particle during the retorting. *Int J Heat Mass Tran.* 2015;84:578–583.
- 93 Jiang X, Han X, Cui Z. Progress and recent utilization trends in combustion of Chinese oil shale. *Prog Energy Combust.* 2007;33(6):552–579.
- 94 Eliyahu M, Emmanuel S, Day-Stirrat RJ, Macaulay CI. Mechanical properties of organic matter in shales mapped at the nanometer scale. *Mar Petrol Geol.* 2015;59: 294–304.
- 95 Chen J, Georgi D, Liu H. Electromagnetic thermal stimulation of shale reservoirs for petroleum production. *J Nat Gas Sci Eng.* 2018;59:183–192.
- 96 Huang J, Xu G, Hu G, Kizil M, Chen Z. A coupled electromagnetic irradiation, heat and mass transfer model for microwave heating and its numerical simulation on coal. *Fuel Process Technol.* 2018;177:237–245.
- 97 Kang Y, Chen M, Chen Z, You L, Hao Z. Investigation of formation heat treatment to enhance the multiscale gas transport ability of shale. *J Nat Gas Sci Eng.* 2016;35: 265–275.